Cancer cell characterization with microfluidic impedance cytometry and neural networks

Dijcks, J.L.

Award date:
2021

Department of Mechanical Engineering
Microsystems Research Group

Cancer cell characterization with microfluidic impedance cytometry and neural networks

Master Thesis

Joris Dijcks
1069276

Supervisors:
Dr. ir. Y.B. van de Burgt
Ir. E.R.W. van Doremaele

Committee:
Prof. dr. ir. J.M.J. den Toonder
Dr. ir. A.J.H. Frijns

Eindhoven, June 11, 2021

Abstract

Circulating tumor cells (CTCs) are a subset of cells found in the blood of patients with solid tumors. Once in the blood, these cells can initiate new metastases (spreading) in other organs, which is the main reason for cancer-related death. Detection of CTCs is a crucial tool in the early diagnosis of cancer. Despite efforts to detect and classify CTCs, no single method seems to be able to handle the detection of CTCs accurately and rapidly.

This project is part of a greater program that exploits the strength of machine learning to efficiently classify CTCs. It sets out to combine a hardware-based neural network with a modular microfluidic chip, where input is generated by a range of integrated sensors optimized for characterizing various cell properties.

To tackle the development of one of these sensors, this work develops an impedance sensor featuring a microfluidic channel with integrated electrodes combined with an experimental measurement setup. By filling the channel with a conductive solution and applying an AC voltage to the electrodes, the impedance is measured as individual cells pass through, revealing the cell's dielectric characteristics.

Polystyrene beads, MCF-7- and MDA-M23- breast cancer cells were passed through the sensor and measured individually. The sensor effectively differentiated polystyrene beads with varying size. By probing the impedance simultaneously at low (200-500kHz) and intermediate(1-5 MHz) frequency, dielectric information regarding the cell membrane capacitance was obtained. This was demonstrated by differentiating between polystyrene beads and cells, as well as between live cancer cells and those with compromised membranes.

The capability of the sensor to offer multiparametric information conveying cell velocity, cell size and dielectric properties, while keeping data processing relatively simple, makes it ideal for neural network implementation. Relevant information was extracted from the raw sensor signal and used to train a simple software-based perceptron neural network, paving the way for future application of hardware-based neural networks.

Contents

1 Introduction

Circulating tumor cells (CTCs) are a subset of cells found in the blood of patients with solid tumors. [1] Once in the blood, these cells can initiate new metastases (spreading) in other organs [2] which is the main reason for cancer-related death [3]. CTCs are particularly useful as a biomarker (medical indicator) for the metastatic state of cancerous tumours within the human body[4]. Detection of CTCs can be used for early diagnosis of cancers, earlier evaluation of cancer recurrence and chemotherapeutic efficacy, and choice of individual sensitive anti-cancer drugs. Therefore, CTC detection is a crucial tool in the fight against cancer.

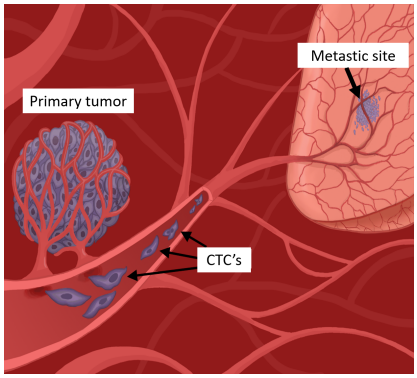

Figure 1.1: Illustration of circulating tumor cells (CTC) forming metastasis. Tumor cells escape from the primary tumor site into the circulation where they can be detected as CTC. Some cells will eventually infiltrate into the surrounding tissue and form a metastic site in other organs. [5]

In contrast to conventional invasive biopsies where tissue is taken from the body, so-called "liquid biopsies", i.e. sampling of blood, can be fast and non-invasive. However, the CTC count in blood is generally very low (1 CTC per mL can be physiologically relevant[6],[7]) which makes these liquid biopsy techniques extremely challenging. Apart from their low prevalence, CTCs exhibit a large morphological and molecular variation adding to the complexity of detection [8]. State-of-the-art techniques, such as fluorescent-based flow cytometry, rely on specific fluorescent or magnetic markers on the cell surface. This additional labeling step is complex, expensive, time-consuming and could lead to sample deterioration [9]. This major weakness emphasizes the urgency for label-free detection methods that are based on inherent cell properties.

An interesting solution to this problem can be found through the electrical properties of CTCs. For example, the dielectric properties of tumour cells differ from normal blood cells [10]. CTCs generally have a larger membrane surface area that features characteristics such as folds and microvilli (portrusions), which create a larger membrane capacitance compared to normal smooth membraned cells. Investigating the dielectric properties could provide other useful information regarding geometry, physiological state, viability and growth while evading labeling [11].

The dielectric properties of cells can be analyzed by applying an excitation voltage (AC) and measuring the resulting current. Impedance, the ratio of the voltage to current signal, expresses opposition to electric current. An effective technique is dielectric bulk spectroscopy, a label-free method, where the impedance of a cell suspension is measured over a range of frequencies, providing information regarding the bulk behaviour of a cell populations. Bulk measurements on a mixture of cells provide averaged information, yet individual cells, which might be indistinguishable in appearance, generally have heterogeneous behaviour [12, 13, 14]. Because of the heterogeneity of individual cells within a population, it is essential to investigate individual cells instead.

To meet this demand, a giant amount of innovations have supported advances in single-cell analysis. Advances in micro-fabrication methods have lead to the manipulation of ever smaller sample volumes ($10^{-9} - 10^{-18}$ litres), allowing researchers to screen single particles at high throughput [15]. Innovations in this field have also been driven by the progress in measurement equipment performance with respect to signal processing, accuracy and versatility.

To achieve accurate, high throughput (10^3–10^4 cells per second) and label-free detection of CTCs, impedance measurements and microfluidics are united in microfluidic impedance cytometry. In a microfluidic impedance chip, cells in a conductive buffer are individually passed through a microfluidic-channel equipped with electrodes that generate an electric field. As a cell disturbs the electric field, the changes in impedance reveal information regarding its dielectric properties[16, 17].

Promising as the results may be, despite various efforts[18, 19, 20, 21] to detect and classify CTCs, no method alone seems to be able to handle the detection of heterogneous CTCs accurately and rapidly. Hybrid systems, where detection methods based on different physical properties are combined to obtain multi-dimensional data, could be beneficial. Combining sensor data with different physical fingerprints will create very large and ambiguous data sets that often require a human check. Recently, various notable research studies have suggested that software based AI can perform better than humans at vital healthcare tasks. Today, algorithms already surpass radiologists at spotting malignant tumours [22, 23], and help researchers improve costly clinical trials[24]. The benefits of machine learning and AI lie in the processing of large datasets and implementation of reliable analysis into clinical insights, improving healthcare and ultimately improving results, reducing costs and saving lives. The detection and analysis of CTCs could benefit significantly from the adaptation of machine learning.

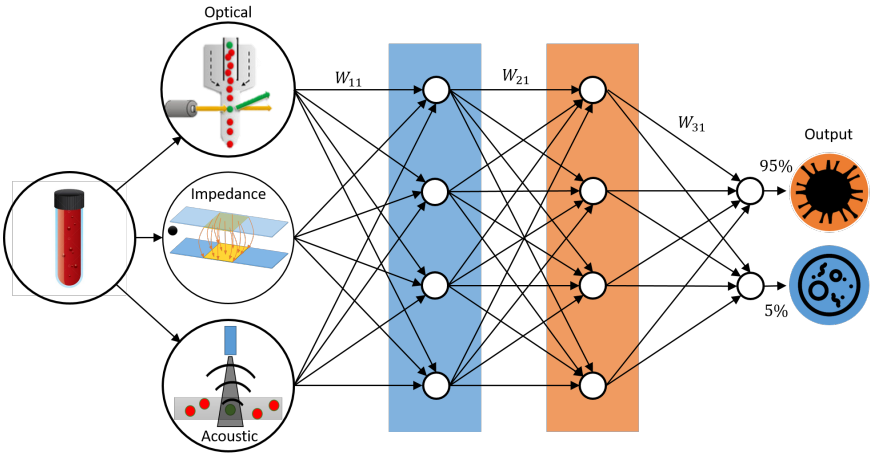

Figure 1.2: Combination of inputs from sensors of different physical nature with a neural network to classify CTC's in a liquid biopsy

Software-based neural networks use conventional von Neuman computing, based on energy intensive and inefficient sequential processing where data is transferred back and forth between the processing and memory units [25]. To execute neural network algorithms at an energy efficiency and interconnectivity comparable to that of the brain, it would be desirable to mimic the brain's synaptic functionality in hardware. Researchers recently introduced an artificial synapse in Nature [26], able to take on and retain a high number of analogue states, ideal for pattern recognition and classification of unstructured (big) data.

The use of different physical sensing techniques combined with the strength of neural networks in hardware can be revolutionary in the classification and sorting of CTCs (Fig. 1.2). The aim of this research is to develop a microfluidic impedance sensor capable of detecting and differentiating cancer cells to train a neural network. As the development of the hardware based neural network is still in progress and out of the scope of this research, it is mimicked by a simple interim software based neural network.

This research will tackle the sensory side by exploring the possibilities of impedance cytometry. It commences with the development of a microfluidic chip capable of manipulating small controlled fluid volumes. This is followed up with the development and integration of an impedance sensor which monitors the impedance of the fluid. Parallel to this, an experimental measurement setup will be established, which controls the fluid flow, generates the electric field and measures the resulting impedance. The dielectric fingerprint of particles and cells, hidden in the raw signal is revealed through signal conditioning and software post-processing. Focus will be on the utility of certain parameters from the impedance signal and its relevance for neural network applications. The multi-parametric impedance data will be used to train a simple neural network in recognizing patterns and distinguishing particles and cells. Starting with differently sized polystyrene beads, it works towards the detection and classification of cancer cells with a simple neural network algorithm. This technology will be developed for future use in a setup where multiple physical sensors will be combined with a hardware based neural network, integrated on a lab-on-a-chip application.

The overall structure of this report is as follows: section 2 focuses on the theoretical fundamentals of impedance, dielectric properties of cells provided with a short introduction on neural networks. Section 3 bridges the gap between theory and practise through modelling. Section 4 provides a description of the device design, fabrication methods, the experimental setup and data analysis. Experimental results are investigated and compared with the simulations in section 5. Finally, section 6 recaps the most important conclusions and provides an outlook for future work.

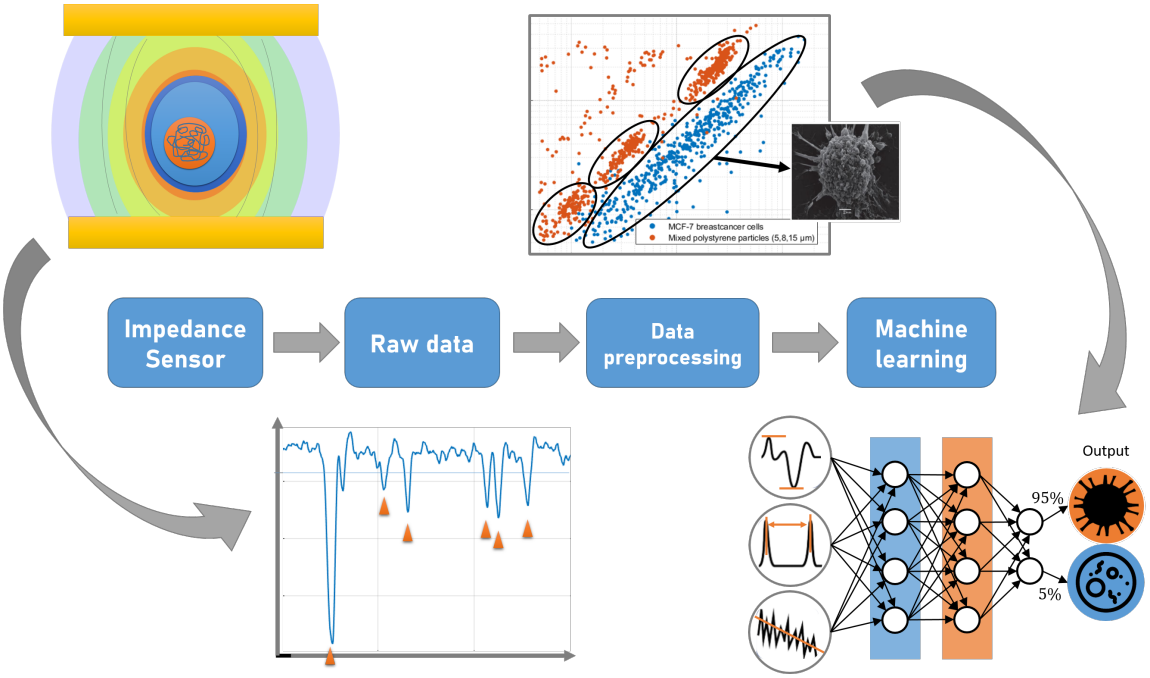

Figure 1.3: The outline of the project.

2 Theory

This project creates a sensor that essentially monitors the dielectric properties of a cell-suspension. This section provides a theoretical foundation on impedance and dielectrics. These subjects are then linked with the dielectric properties of particles and cells. This is followed up with two ways of describing the dielectric behaviour of the system with theoretical models. This section is finalized with a short introduction on neural networks.

2.1 Electrical Impedance

Electrical impedance is defined as the ratio of the voltage to an alternating current (AC) passing through a system, i.e. obstruction of an AC flow [27]. Impedance takes the concept of a resistance, which is independent of frequency, and extends it with "reactance". Reactance is the opposition to current due to the concepts of capacitance and conductance, which depend on frequency. Impedance, Z, is a general term for the contribution of the resistance and reactance:

$$Z = \underbrace{R + jX}_{\text{Cartesian form}} = \underbrace{|Z|e^{j\Phi}}_{\text{polar form}} \tag{2.1}$$

Where the real part, R, represents the resistance and the imaginary part, X, the reactance. j is the imaginary unit. $|Z|$ is the magnitude of the impedance. The phase angle Φ is the difference between the phase of the voltage and the phase of the current. A visual representation is given in figure 2.1A.

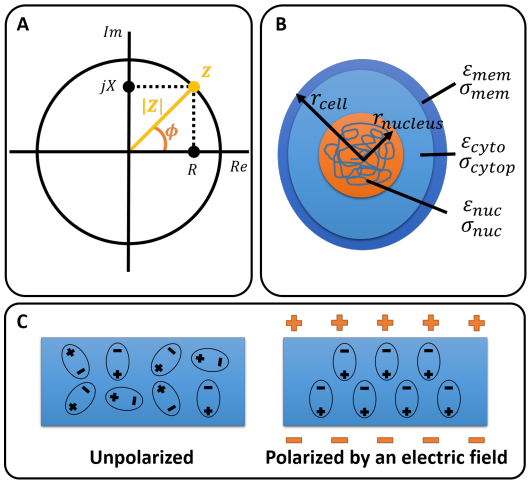

Figure 2.1: (A) A graphical representation of the electrical impedance. (B) Graphic of the structure of a "typical"cell describing the outer membrane, the inner fluid between the membrane and the nucleus. (C) A graphical representation of the dipole moments in a polarizable material.

2.2 Dielectric properties of particles and cells

A dielectric is an electric insulator, meaning non-conductive under the influence of an electric field, but polarizable by that same electric field [28]. A polarizable material contains random oriented molecules, which have an non-homogenous distribution of electrons, where one end of the molecule is slightly positive, while the other end is slightly negative. When an electric field is applied, the dipole moments of these molecules are shifted from their original position, see figure 2.1C. They are aligned in such a way that an internal electric field is formed, which reduces the overall electric field within the dielectric itself. This will increase the energy storing capacity.

This process is called dielectric polarization and the polarizabillity of a dielectric material is termed permittivity.

Polarization is not an instantaneous process. A lag between changes in polarization and the electric field, termed dielectric relaxation, is present. This creates a dependence on the frequency of the applied electric field. The dielectric relaxation response of a population of dipoles in a medium, i.e. its frequency dependence, is expressed in the complex permittivity η:

$$\tilde{\varepsilon}(\omega) = \varepsilon_\infty + \frac{\Delta\varepsilon}{1 + i\omega\tau} \tag{2.2}$$

where ε_∞ defines the permittivity at very high frequencies, $\Delta\varepsilon = \varepsilon_s - \varepsilon_\infty$ with ε_s being the low frequency permittivitty and τ the characteristic relaxation time of the medium. If the frequency of the electric field increases to such a degree that the dipole moments in the material can no longer follow the oscillations, the process loses its response, the energy storing capacity and the permittivity both decrease. The dependence of the permittivity on frequency is described by dielectric dispersion.

Biological cells are not homogeneous, but consists of a complex composite material with varying electrical properties, see figure 2.1B. To describe the underlying dielectric mechanisms, Pauly [29] developed a simplified 'single shell' model, consisting of a plasma membrane surrounding a cytoplasm. The membrane is a lipid layer consisting of proteins. Because of its low ionic permeability it is considered a low conductive thin shell. Schwan [30] defined three discrete dispersion regions for cells in suspension:

- α- dispersion (10 Hz - 10kHz) attributing to the polarization of the electric double layer around the cell. The α- dispersion is hard to investigate due to the electric double layer at the electrode interface dominating the impedance at low frequency.
- β- dispersion (1kHz - 1Mhz) associated with the interfacial polarization of the capacitive cell membrane. If the frequency reaches a certain value and the cell membrane capacitance is electrically "short-circuited", current can penetrate into the cytoplasm which would result in a drop in overall impedance.
- γ- dispersion ($>$ 1Mhz) occurs due to the dipolar relaxation of water molecules

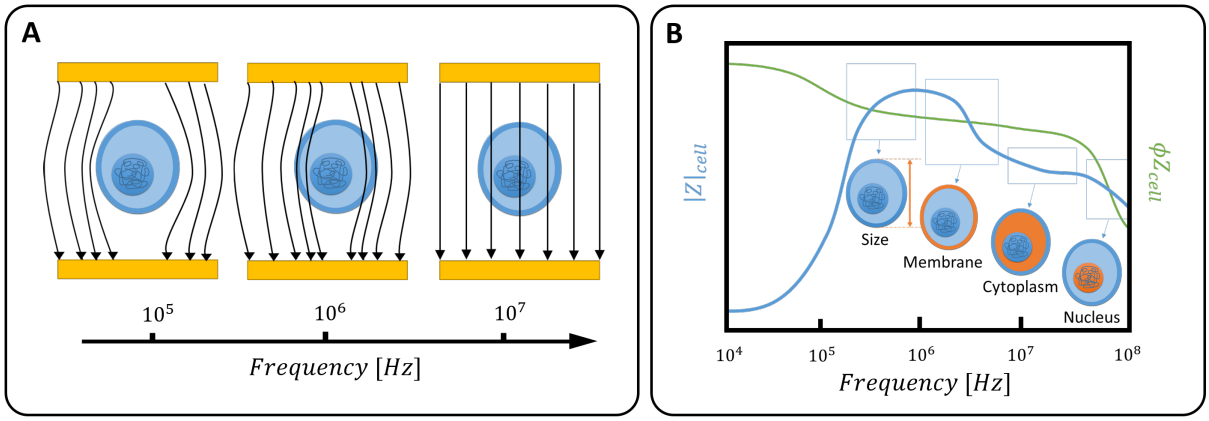

Figure 2.2: (A) As the frequency is increased, different cell components dominate the impedance of current. (B) The approximate variation in magnitude and phase of the impedance spectra of a cell. Based on a model of Sun et. al[12]

Revealing the dielectric characteristics of a cell by shifting the frequency over the different dispersion regions and probing the resulting impedance is a very powerful and non intrusive way of cell analysis.

To conclude, at low frequency, the cell membrane acts as a barrier to current flow and measuring the impedance gives an indication of volume or size[31], see figure 2.3A. Particles of the same volume but different dielectric properties would not be differentiated with measurements at low frequencies. Increasing the frequency gives the dipoles less time to attain full polarization. Impedance measurements at intermediate frequencies, provide information on the membrane characteristics. At relatively high frequency, the dipole moments in the membrane have insufficient time to align and current effectively passes the membrane. Impedance measurement at these frequencies reveal information about the heterogeneous structure and intracellular dielectric properties. Figure 2.3B gives an approximation of the variation in magnitude and phase of the impedance with frequency for a cell, based equivalent circuit modelling [12].

This project focuses on cancer cell characteristics and their corresponding dielectric properties. These have been subjected to extensive research in the past [32, 33]. The dielectric properties of cancer cells are different compared to normal mono-nuclear blood cells [34, 10]. The main discrepancy can be found in the membrane. Cancer cells have a rough and large membrane surface area with folds and small microvilli, which are small microscopic protrusions. This translates into an increased membrane capacitance in comparison with an equally sized cell with a smoother membrane. Another characteristic of a cancer cell is a slightly higher nucleus-to-cytoplasm ratio [11, 35] and cell cycle turnover[11, 36], both of which influence the cytoplasm conductivity.

2.3 Maxwell Mixture theory & the equivalent circuit model

The sample flowing through the microfluidic channel is a mixture of medium and particles. The electrical behavior of this mixture under the influence of an electric field can be described with Maxwell's mixture theory[37, 38, 17, 39]. This theory relates the complex permittivity of the mixture to that of the cell, the suspending medium and the volume fraction.

As shown in figure 2.3A, Maxwells's theory shows a direct relation between the mixture impedance, Z_{mix}, the geometric properties G_f, and dielectric properties of the system, $\tilde{\varepsilon}_{mix}$. The complex permittivity of the mixture is directly related to the volume fraction, medium permittivity and the Clausius-Mossotti factor. The Clausius-Mossoti factor $\tilde{f}_{CM}$ describes the frequency-dependent effective dipole moment that gives rise to the dielectric behaviour. This factor is based on the complex permittivity of the cell and is computed with appropriate single- or multi-shell models [40, 39]. Box C in figure 2.3 relates the cell permittivity to the individual membrane and cytoplasm properties.

An assumption is that the volume ratio between the cell and the suspending system, is small ($\phi < 1$) and that the cell membrane thickness, d, is much smaller than the cell diameter, r. G_f is the ratio of electrode area to electrode gap for an ideal parallel electrode plates with a homogeneous electric field. Applying this model for a co-planar sensor, where the electrodes are next to each other in a channel, this factor compensates for non-homogeneous electric field distribution and fringing effects [16]. A more extensive derivation of Maxwell's mixture theory, can be found in the appendix A.

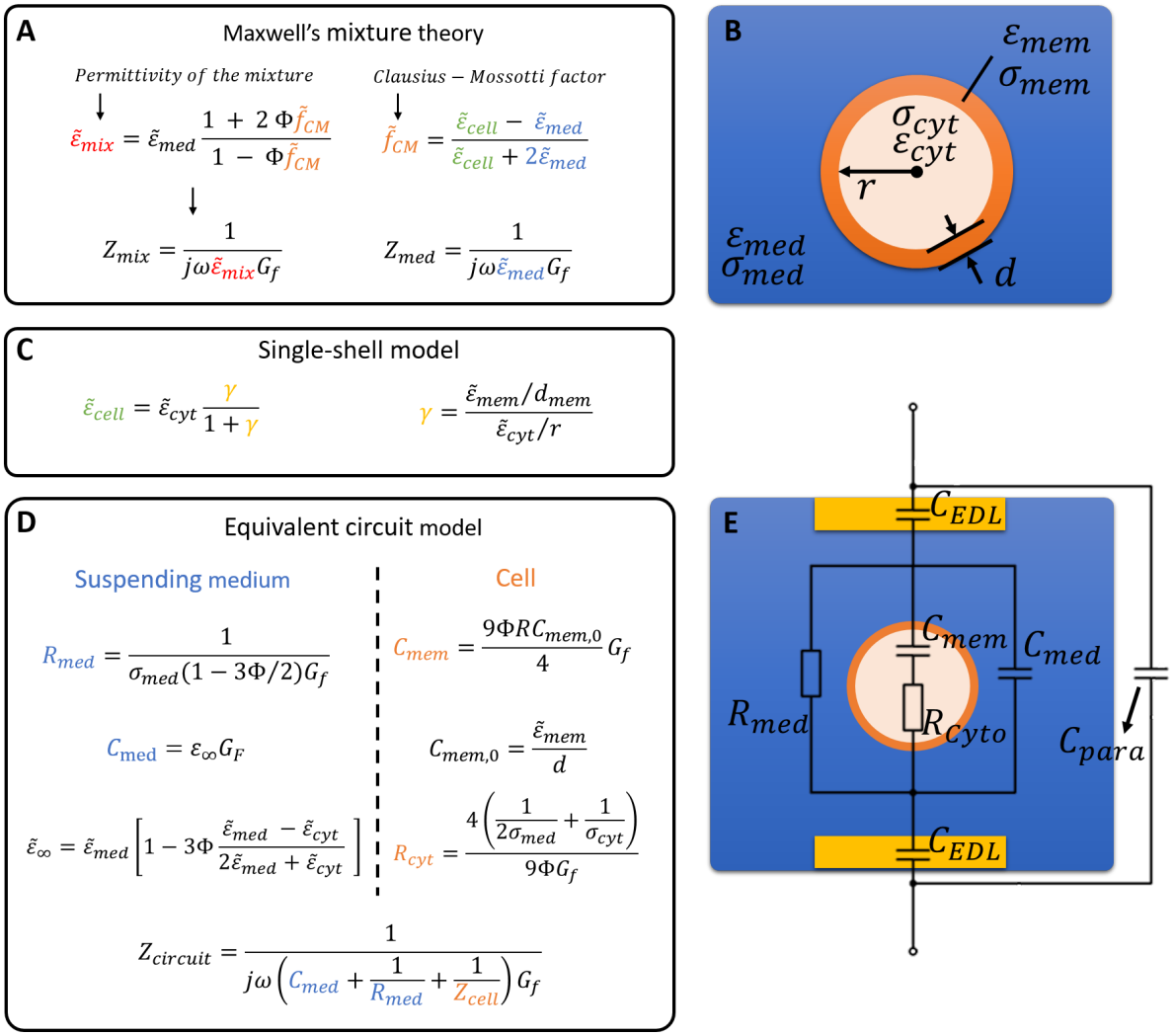

Figure 2.3: (A) Maxwell's mixture theory (B) Extension of Maxwell's equations with a single shell model. (C) Equivalent circuit formula's for each component and the circuit as a whole

Maxwell's mixture theory forms the foundation for equivalent circuit modelling. The dielectric properties of biological materials incorporated into an equivalent circuit model was first developed by Foster and Schwan [41]. It explains the behaviour of each components within the system and the system behaviour as a whole. Figure 2.3D and E describe the simplified electrical circuit of a sensor with a cell present in the electric field between two electrodes. The open connections to the system are indicated with lines ending with open rounds located at the top and bottom side. The C_{EDL} represents the electrical double layer at the electrodes. C_{medium} and R_{medium} describe the capacitance and resistance of the medium in the detection area between the electrodes. To approximate the general behaviour of a cell in an electric field, it can be modeled simply as a resistor that describes the cytoplasm, R_{cyto}, in series with a capacitor for the membrane, C_{mem}, as shown in figure 2.3E [16]. The cell membrane resistance is generally much greater than the capacitance of the membrane and can therefore be ignored[17, 39]. The cytoplasm capacitance is generally much smaller than the resistance and can therefore also be ignored. $C_{parasitic}$ represents a constant parasitic (stray) capacitance, which is unavoidable and related to the proximity of measurement equipment and cabling. σ_{med} is the conductivity of the medium, Φ is the volume fraction of the cell to the detection volume and G_f is the ratio of

electrode area to electrode distance. $C_{mem,0}$ is the specific membrane capacitance. The limiting high-frequency permittivity of the suspension, $\tilde{\varepsilon}_\infty$, is related to the suspending medium- and cytoplasm permittivity.

2.4 Neural network classification theory

The information that is acquired from the impedance sensor will be labeled and used to train a simple neural network algorithm that classifies particles. The network is trained through classifiers, which are functions that decide whether an input belongs to a certain class. The algorithm, also called a perceptron, is a feed-forward network that starts with multiplying the input values with their randomly assigned weights. A weight, is a parameter that scales the values of the inputs. The values of these multiplications are then summed up in the weighted sum. The weighted sum is applied to a hard-limit activation function that maps an input to an output value and returns an output of a 0 or 1. The hard-limit transfer function gives the perceptron the ability to classify input vectors by dividing the input space into two regions. The algorithm finds a line that correctly separates the two classes by tweaking the weights and biases after each loop. The procedure of adjusting the weights after each loop is governed by the "learning rule". In the case of supervised learning, the learning rule is given a training set where the inputs are given a corresponding target output. As the inputs are inserted into the network, the output is compared to the target. The learning rule then adjusts the weights and biases of the network based on the difference between the target and output, which is the error. This way the network brings the outputs closer to the target. The limitation of this perceptron algorithm is that it can only separate input vectors that can be separated by a linear boundary. Additional theory and a full explanation of perceptrons with an extension to multi-layer perceptron networks can be found in appendix B.

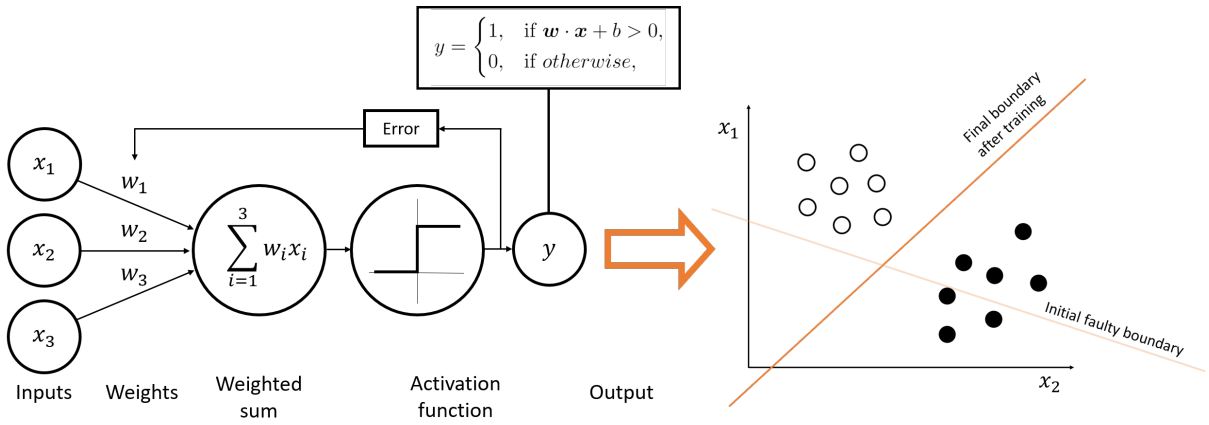

Figure 2.4: Perceptron neural network with three input vectors, their assigned weights, the weighted sum, the hard-limit activation function, the error from the target that adjusts the weights after each loop, and finally one binary output. On the right side, the algorithm starts out with an line constructed with random weights and bias. After each loop the weights and biases are adjusted to minimize the error and readjust the line until convergence

3 Modelling

In reality, the impedance sensor is a complex system where different physical phenomena take place. This section aims to make particular physical mechanisms of the whole system easier to understand and visualize. A simplified numerical COMSOL model provides a basic understanding of the underlying physics and illustrates how design choices like the channel geometry, electrode designs, and experimental conditions affect the performance of the sensor. Another tool to better understand the system is the modelling of an electrical circuit which is analogue to the electrical behaviour of a particle-suspension under the influence of an electric field. This section will give a short overview of the most interesting results, a complete description of the models and elaboration on all other results can be found in the appendix C

3.1 COMSOL model

This simple model illustrates how the channel geometry, electrode designs, and experimental conditions affect the sensitivity of the sensor. The COMSOL model simulates a particle travelling through a microfluidic channel, disturbing the electric field between two co-planar electrodes, thus creating a change in impedance. An overview is depicted in figure 3.1a. The influence of the following parameters are investigated: the inter-electrode distance d_{el}, the width of the electrodes w_{el}, the particle material properties, geometry and vertical trajectory position, the medium properties properties and the channel geometry.

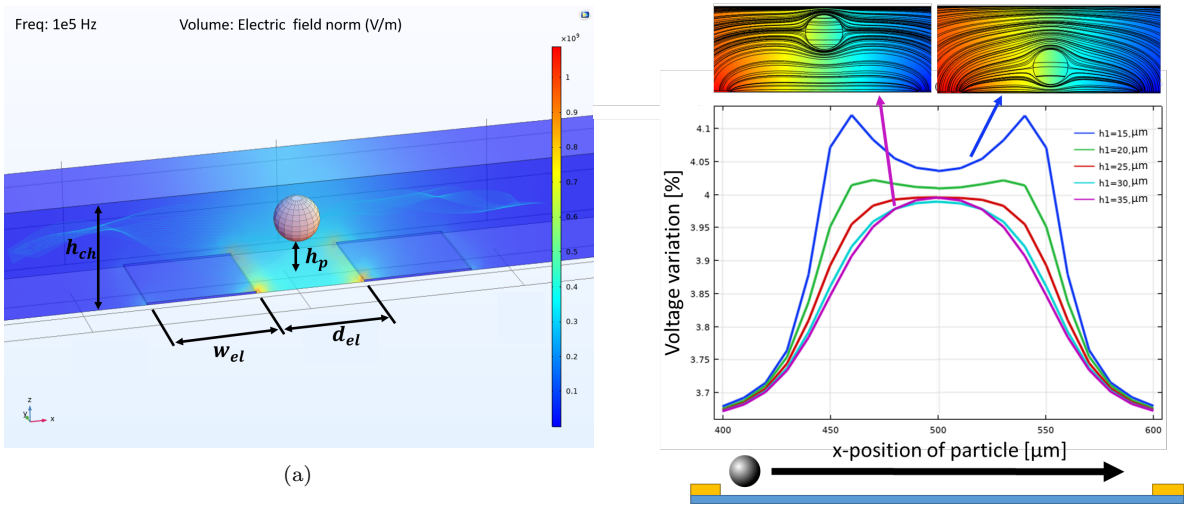

(a) (b)

Figure 3.1: **(a)** 3D model including the normalized electric field intensity of the detection volume with the design parameters. **(b)** Simulation of the voltage variation as the particle vertical position is changed

3.1.1 Positional dependence

Figure 3.1b shows the voltage variation as a particle passes through the electric field. The simulation reveals the influence of the vertical particle position within the channel. A particle just barely passing over the electrodes, where the current density is higher, results in a larger signal variation. It causes two distinct peaks, compared to the single peak when the beads pass at a higher position in the channel.

3.1.2 Electrode geometry

Figure 3.2 simultaneously shows the effects of the electrode distance d_{el}, vertical particle position, and particle size on the voltage variation. Noteworthy is the increased signal variation that scales with the sphere volume and the significantly higher signal variation for a d_{el} of 50 μm compared to a d_{el} of 150 μm. The fact that besides the width of the peak being much wider for a larger d_{el}, a larger d_{el} decreases the sensitivity to vertical particle position. The signal variation in the central zone (x=0 μm) varies little and hence will depend mostly on the size of the particle. To a degree, by increasing the electrode width, the sensitivity is decreased but positional dependence on the signal could be neutralized.

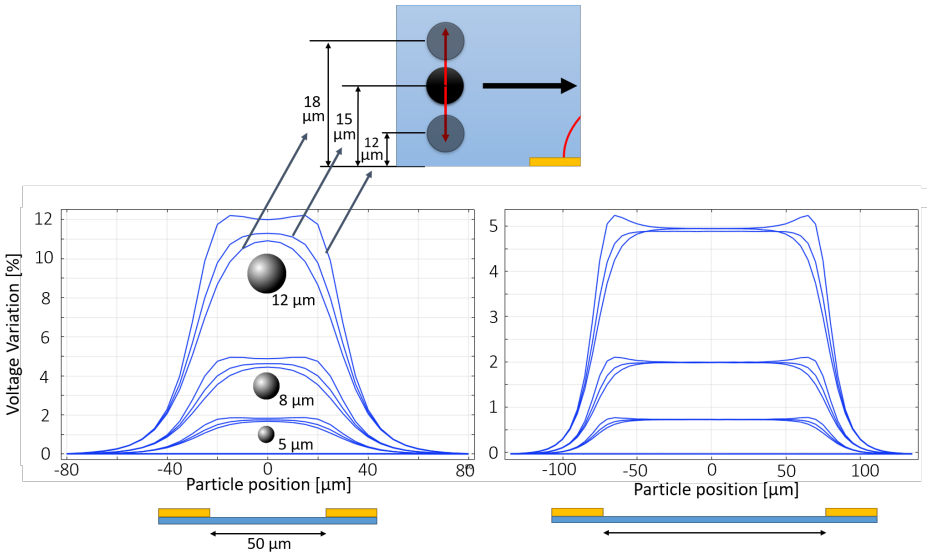

Figure 3.2: The impact of electrode distance on impedance variation

3.2 Equivalent circuit simulations: device characterization

The theoretical equivalent circuit model in section 2.3(box D) and other models[42] form the basis for this section. When considering the simplified electrical circuit of the device without a cell in figure 3.3a, the total impedance roughly depends on 3 components: the medium resistance, the capacitive electric double layer at the electrode surface and the medium capacitance:

$$Z_{circuit} \approx \frac{x}{j\omega C_{med} x + 1}, \quad x = R_{sol} + \frac{2}{j\omega C_{DL}} \tag{3.1}$$

For simplicity the parasitic capacitance present in the cabling and equipment is ignored. To investigate the influence of these 3 components on the impedance of the system, a model was created in LTSPICE, which is an analog electronic circuit simulator software program. The goal of the model is to create an understanding on the interaction between the components. It provides a guideline for device design and helps with the interpretation of experimental results.

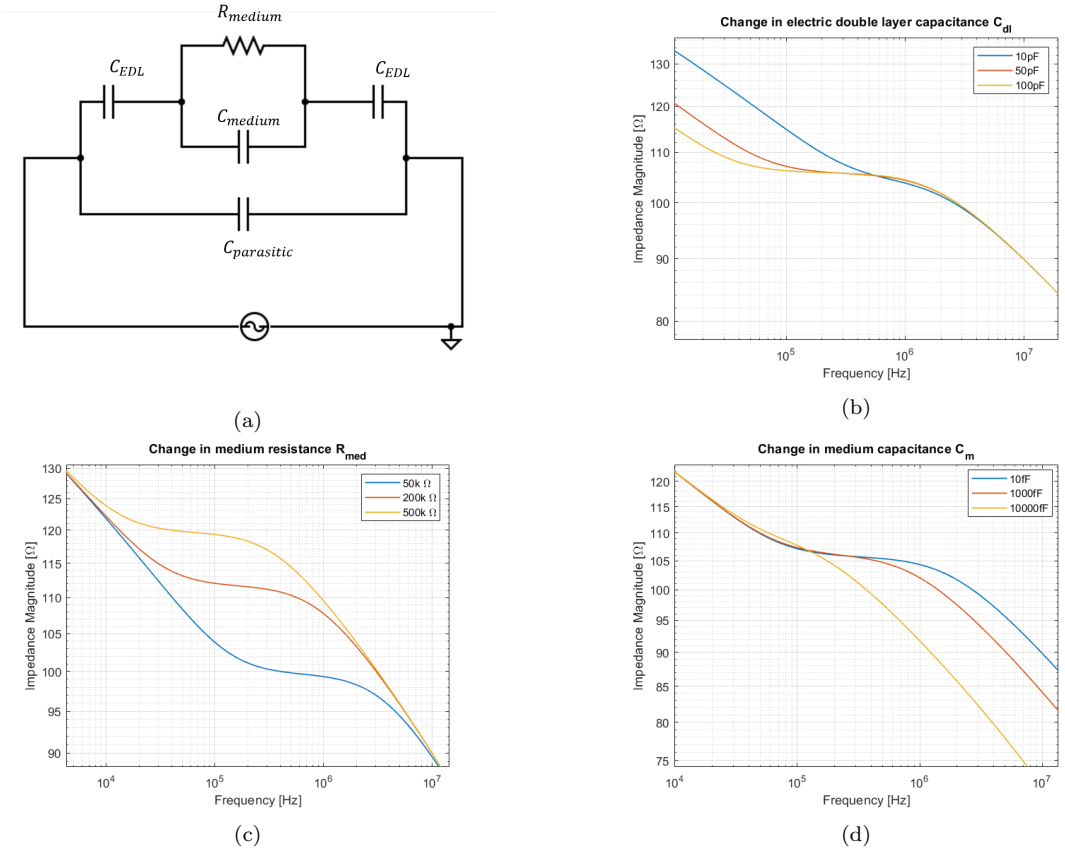

Figure 3.3: The influence of a changing. **(b)** double layer capacitance. **(c)** medium resistance. **(d)** medium capacitance

The circuit in figure 3.3a was modelled in LT spice and the values of each component were changed to see the influence on the spectrum. The impedance of the system has three important frequency regions. Each frequency region corresponds to one or more components in the equivalent circuit model. The low frequency region is dominated by the double layer capacitance at the electrodes, being the main contributor to the impedance. It acts as an open circuit and no current flows. When the frequency increases, the impedance due to the electric double layer decreases. If the point is reached where the impedance of the electric double layer equals the impedance of the medium resistance a transition into the second region occurs:

$$f_{low} \approx \frac{1}{R_{med} C_{DL}} \tag{3.2}$$

When the frequency reaches f_{low} the double layer capacitors are "short-circuited" and the medium resistance becomes dominant. The medium acts as a resistor, which is independent of frequency and results in a resistive plateau. This resistive plateau is the region where unbiased impedance measurements are possible. If the frequency increases further, the impedance of the medium capacitance drops below the impedance of to the medium resistance and the last region occurs. The transition is approximated by:

$$f_{high} \approx \frac{1}{R_{med} C_{para}} \tag{3.3}$$

When the frequency reaches f_{high}, the impedance drops further because the medium capacitor short-circuits, see figure 3.3d. The impedance then becomes inversely proportional to the

frequency. In experiments, the first region, dominated by the electric double layer capacitance correlates with electrode area and electrode surface roughness. Increasing the capacitance of the double layer, for example through larger electrodes, could extend the resistive plateau, as seen in figure 3.3b. When the medium resistance is varied, only the location of the plateau will shift according to figure 3.3c. The resistive plateau is also extended by decreasing the medium capacitance, see figure 3.3d.

3.3 Equivalent circuit simulations: the cell model

To approximate the general behaviour of a cell in an electric field, it can be modeled simply as a resistor that describes the cytoplasm in series with a capacitor for the membrane [16]. The cell membrane resistance is generally much smaller than the capacitance of the membrane and can therefore be ignored. The cytoplasm capacitance is generally much smaller than the resistance and can therefore also be ignored. Figure3.4a, shows the electrical circuit as modelled in LTspice. A differential configuration is simulated to highlight the effect of the cell in the electric field and remove the impact of the medium properties on the electric field. The left electrode pair depicts the equivalent circuit for the detection region without a cell compared to the right electrode pair which has a cell in the between. The difference between these two circuits reveals the behaviour of the cell. The impedance magnitude of an insulated polystyrene bead with a high resistance and capacitance is compared to a similarly sized cell with lower resistance and capacitance. The values from literature [43, 44] are tweaked to more resemble the device in this work. The medium resistance and capacitance are 35.38 e-15 F and 14.30 e3 Ω. The electric double layer is modelled as a relatively high capacitance of 200 e-12 F. The bead capacitance and resistance are e-16 F and 120 e5 Ω respectively. The cell capacitance and resistance are 6 e-16 F and 90 e5 Ω respectively. Figure 3.4b shows the differential impedance magnitude between the two electrode pairs. At low frequency, the difference between bead and cell is negligible. The differential signal for the cell drops off at a lower frequency compared to the bead. This is related to the larger impedance (reactance) decrease of the cell capacitance in comparison with the bead capacitance. In cell experiments, this steeper decrease in impedance would correlate with the $\beta-$ dispersion, i.e. the dielectric relaxation of the membrane. The figure includes a rough graphical indication of the frequency regions where each cell structural component would affect the impedance signal according to literature [12, 43].

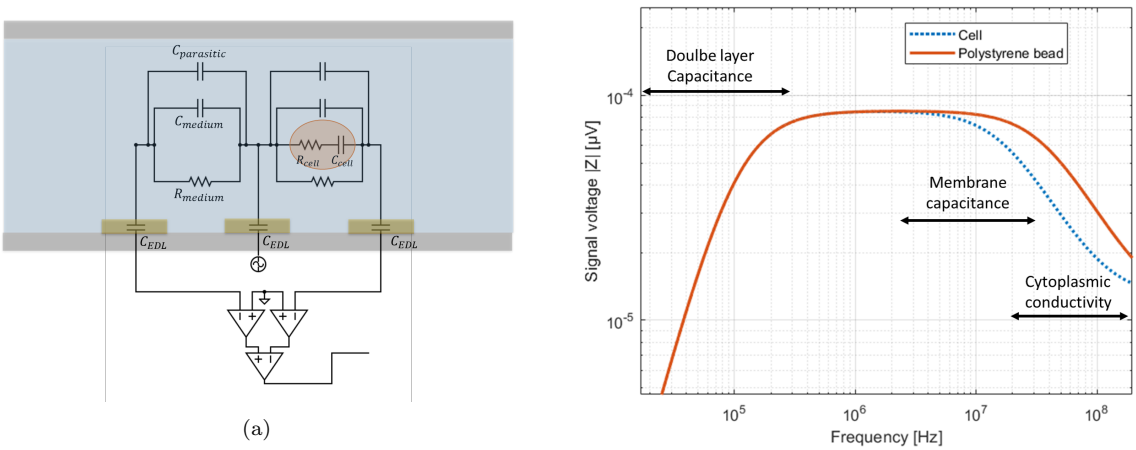

(a) (b)

Figure 3.4: **(a)** The circuit as modelled in LTSpice, the amplification components are ignored for this simulation. **(b)** The impedance magnitude frequency spectrum of a cell compared to a particle

4 Materials and methods

4.1 Device design

In an impedance based microfluidic chip, cells in a conductive buffer are transported through a micro-channel equipped with electrodes. The two most prevalent electrode configurations are co-planar and parallel facing electrodes(REF). In this project a co-planar electrode configuration was chosen for its simple fabrication process, as the bottom glass plate with electrodes and a top layer of PDMS containing the microfluidic channel features requires only one single alignment step. In a design with facing electrodes the PDMS (or similar material) is sandwiched by two glass electrode plates, requiring two alignment steps.

The main disadvantage of the co-planar design is the non-homogeneous electric field distribution within the channel that creates a dependence on particle trajectory position. Solutions to this problem are (hydrodynamic) particle focusing or channel dimensions down-scaling. By decreasing the channel dimensions the ratio between cell and detection volume is increased as well as the resulting impedance change. Naturally, clogging becomes more prevalent and the possible range in cell/particle size is limited.

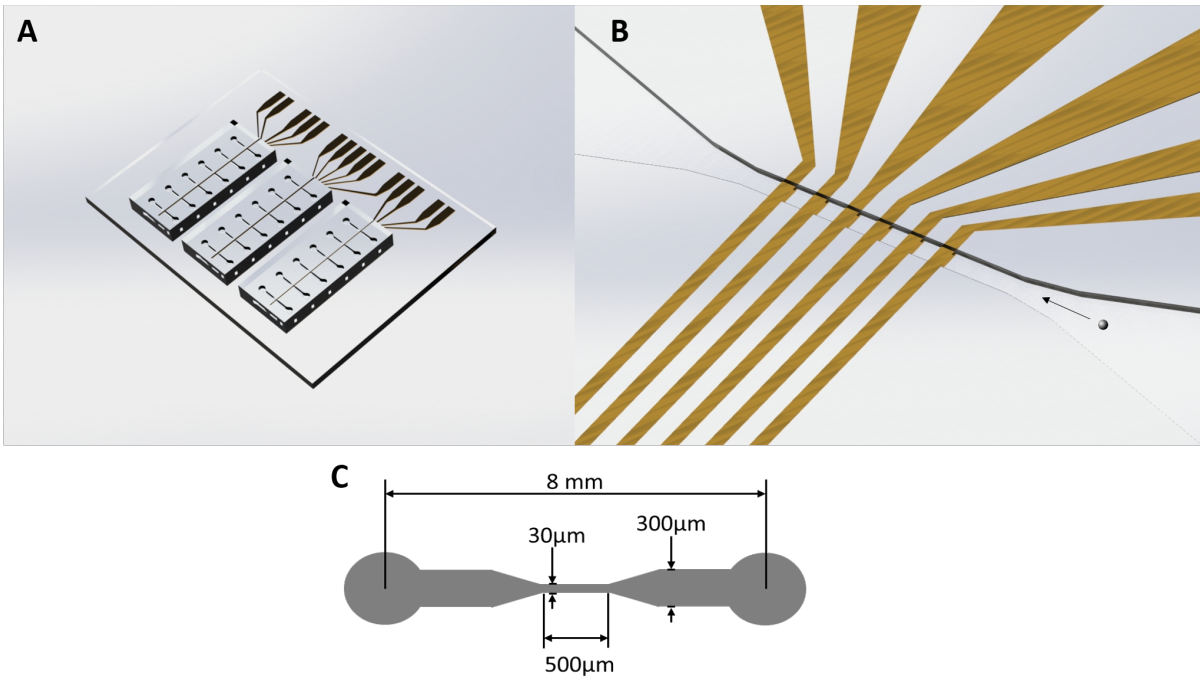

Figure 4.1: **(A)** 3D render of the device, **(B)** Detail of the constriction channel, **(C)** dimensions of the microfluidic channel.

To achieve better results, multiple parameters of the co-planar microfluidic impedance cytometer were altered and investigated. In terms of of channel geometry, the width was varied between 30 and 50 micrometer, while keeping the height constant at 20 micrometer. The length of the small constriction channel is 500 micrometer. The distance between the electrodes was varied between 15,20,30,40,50 and 100 micrometer and the electrode width was varied between 15, 20, 30 and 50 micrometer. The electrode thickness was kept constant at 55nm. Practical issues, like clogging and electrode degradation during testing lead to the multi-channels design in figure 4.1. It depicts a microfluidic chip with 24 channels and 15 electrodes, effectively producing 24 sensors

on one chip. Next to simple two-electrode measurements, this multi-electrode design allows for differential measurements where the difference between two electrode pairs is measured. A differential measurement removes the impact of the environmental properties and measures the cell properties directly against the surrounding media.

4.2 Device fabrication

Creating an impedance sensor that is sensitive enough to distinguish cell characteristics stands or falls with the quality of the fabrication process. In pursuit of the smallest electrode features possible, a glass wafer is rigorously cleaned and irradiated with UV-ozone before a thin layer of negative photoresist (AZ-Nlof 2035) is spun on. After a soft bake the photoresist is exposed by 115 mW/cm^2 with UV-light, followed by a post-bake and development step. Subsequently, a thin 5nm layer of Chromium and a 100nm layer of gold is deposited by sputtering. The resulting electrode features are revealed by lift-off in acetone.

The microfluidic channels are obtained by pouring an elastomer(PDMS, Sylgard 184, Dow Corning, Base to Curing Agent weight ratio 10:1) over a master mould structure, which is then cured in an oven, released from the mould and provided with holes for tubing. The master mold is made by spin-coating a thin layer of SU-8 photoresist on top of a silicon wafer and subsequently baking and exposing it to UV-light before post-baking and development. The device is finalized by alignment under a stereo microscope and bonding of the PDMS channel layer and electrodes with a plasma treatment.

4.3 Experimental setup

In conjunction with the microfluidic impedance chip, the development of the measurement setup build around the device is equally important. A schematic of the experimental setup is shown in figure 4.2. To establish a sample flow, the computer controls the buffer is pumped by means of a pressure driven pump (Fluigent MFCS-EX) or a syringe pump. The microscope gives visual feedback on the proceedings in the chip, which is used to correlate the visual to the electrical events. The lock-in amplifier is used to generate the electric field measure the impedance signal. All these devices are connected to the PC.

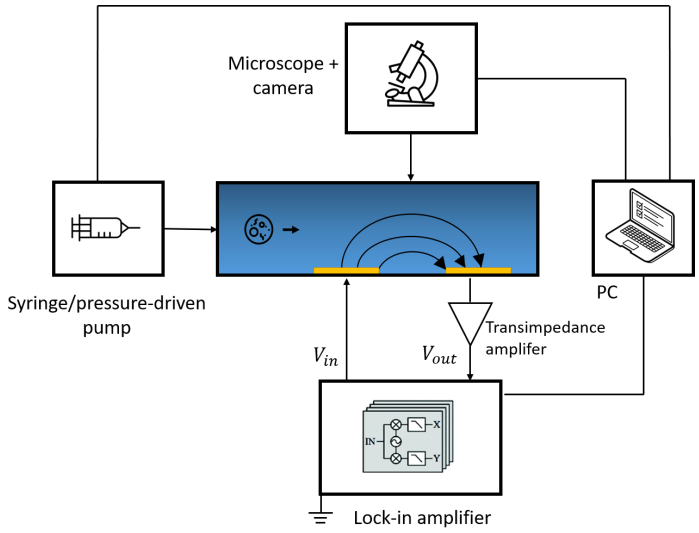

Figure 4.2: Overview of the setup.

4.4 Lock-in amplifier impedance measurement

The cornerstone of the setup is the lock-in amplifier. It is very effective at extracting weak signals from a noisy environments. Figure 4.3 shows the core principle that revolves around demodulation, which is the multiplication of an input with a reference signal followed with a low-pass filter. This multiplication isolates the signal at the frequency of interest, while blocking all other frequencies. The outputs X and Y represent the (real) in-phase and (imaginary) out-of-phase component of the signal. These can be converted into the magnitude and phase of the signal. To establish multi-frequency electric field in the channel, AC excitation signals (1V) of different frequencies are generated and mixed by the internal oscillator of the lock-in amplifier and applied to the electrode. When a particle disturbs the electric field, a change in current is measured. The outgoing current is then amplified with a factor of 1000 and converted to a voltage by the trans-impedance amplifier(HF2TA). The lock-in amplifier simultaneously generates, conditions and demodulates the signals of 6 different frequencies and provides the in-phase and out-of-phase components with a sampling rate of 28750 sa/s.

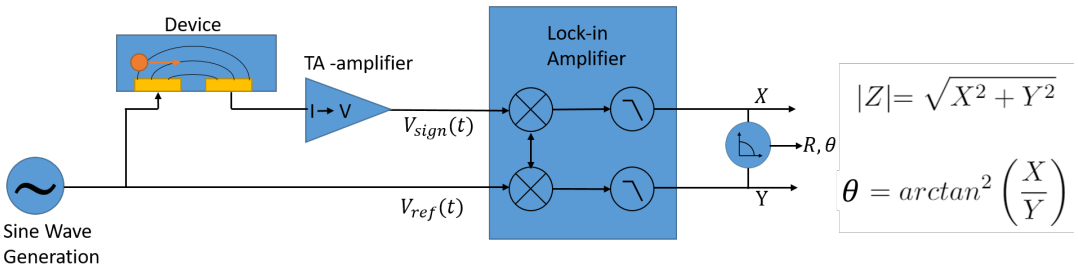

Figure 4.3: Overview of the lock-in detection in during an experiment

4.5 Medium preparation

PBS (Phosphate buffered saline, Sigma-Aldrich) [45]is a water based electrolyte which is similar with respect to osmolarity and ion concentration to body fluids of mammals. PBS has a density of 1.00-1.01 g/ccm and conductivity of 1.6 S/m. Plain spherical polystyrene beads [46], beads with COOH-coating and magnetic polystyrene matrix beads were used in experiments. The plain and COOH-coated beads have a density of 1.03 g/ccm and the magnetic beads have a significantly higher density of 1.1 g/ccm. The amount of beads ranges from 110000 beads per ml for 15 μm beads to 500000 beads per ml for 5 μm beads. Bead diameters are 5, 8, 10, 12 and 15 μm.

MDA-MB231 and MCF-7 epithelial cancer cells were grown in RPMI, a growth medium for mammalian cells. During weekly passage, cells for experiments were extracted by adding Trypsin, detaching them from the petriflask surface. Subsequently the cells are centrifuged and re-suspended in PBS before pumped through the impedance sensor.

4.6 Data Analytics

The lock-in amplifier is connected to the PC using a USB-connection. Figure 4.4 shows a visual representation of the data analysis process from raw impedance data to clean metrics, ready to use for machine learning applications. In MATLAB, the impedance data, either in R and θ or X and Y, is compensated for drift and normalized through a moving average-filter. Subsequently, events in the form of local maxima, above a certain threshold and prominence, are extracted with with a peak finding algorithm. The threshold is chosen manually after each experiment

to separate relevant events from artefacts, noise and debris. Timestamps, peak amplitude and peak widths from data streams with different frequency and microscope videos are synchronized and then further investigated through plots or used to train a neural network. The script and an in-depth analysis exploring the trade-off between different conditioning methods regarding optimal feature extraction and minimizing the loss of information can be found in the appendix E.

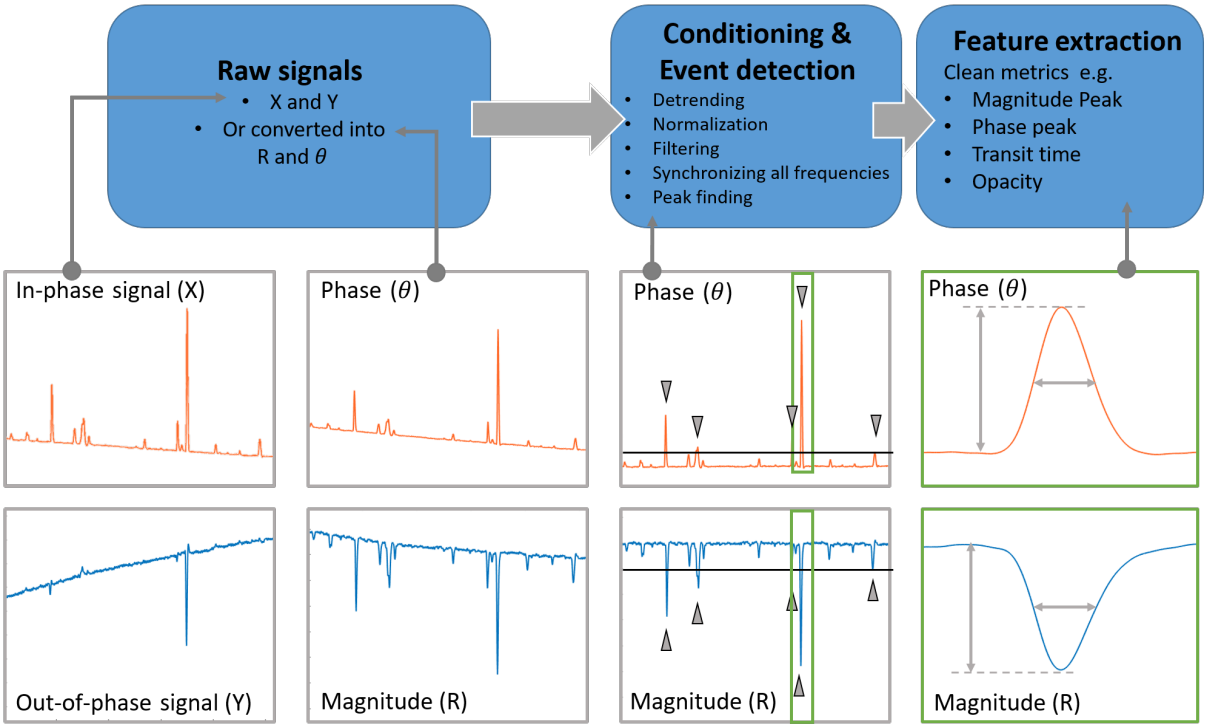

Figure 4.4: A schematic showing examples of the data analysis process from raw data from the lock-in amplifier to clean metrics, ready to use for machine learning

5 Results

Henceforth, all experiments are done with the following microfluidic impedance sensor design until stated otherwise: a 30 μm channel width, 20 μm channel height, electrode width of 20 μm and electrode spacing of 40 μm.

5.1 Impedance measurement & event detection

As the mixture is pumped through the microfluidic channel and a voltage is applied to the single pair electrodes, current flows and an electric field is generated. Passage of a particle over the electrodes and through the electric field, results in an impedance change in the detection area. Figure 5.1 shows the raw magnitude of the signal measured with the Lock-in amplifier of an experiment where a PBS solution with 15 μm beads is pumped through the sensor with a low bead velocity of 200 μm/s.

Describing the signal in the polar form, the detail of figure 5.1 shows the change in signal magnitude as a 15 micrometer particle disturbs the electric field with a signal to noise ratio, $(|Z|_{peak}/|Z|_{baseline})^{-1}$, of around 1.06. Baseline drift in the signal complicates signal analysis and is removed by means of passing the raw signal through a moving average filter and subtracting it. The result is a stable normalized baseline, details are further explained in section 5.2.4. The two extracted features of the inverse peak are its depth and its width. The depth is a measure of change in signal magnitude and the width the duration of the event, i.e. the transit time of a particle. Additional to a change in magnitude, an event may cause a change in phase, see figure 5.2b. Likewise, this change in phase takes the shape of a peak or depression. Figure 5.2a gives a visual representation of the event in figure 5.2b. Z_0 indicates the baseline impedance and Z_e indicates the impedance at the time of an event. Depending on the dielectric characteristics of the particle, Z_e could be positioned anywhere on the plane. If instead of extracting data from the signal in its polar form, occasionally features are brought to light by examining the in-phase (real) and out-of-phase (imaginary) components separately.

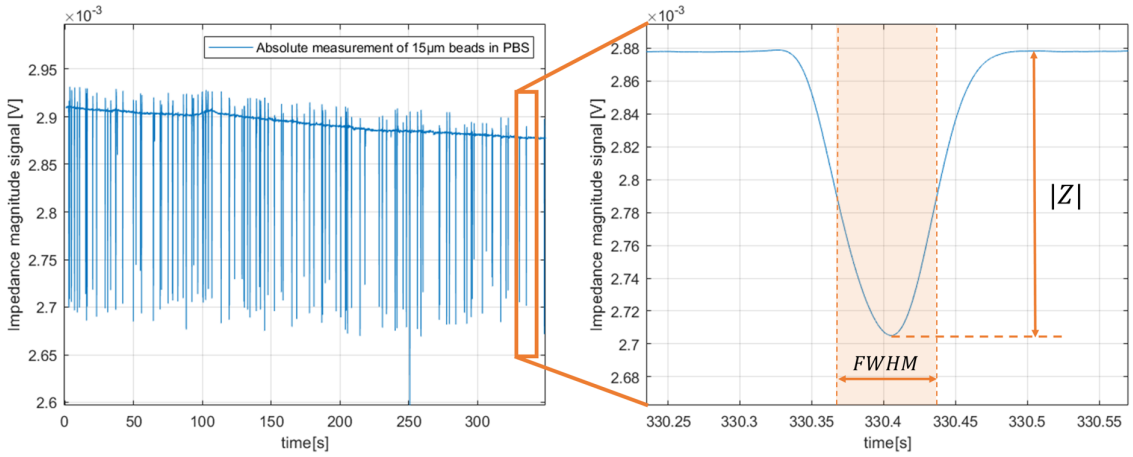

Figure 5.1: Raw impedance magnitude signal of an experiment with 15 micrometer beads with a detail of an event in the shape of an inverse peak

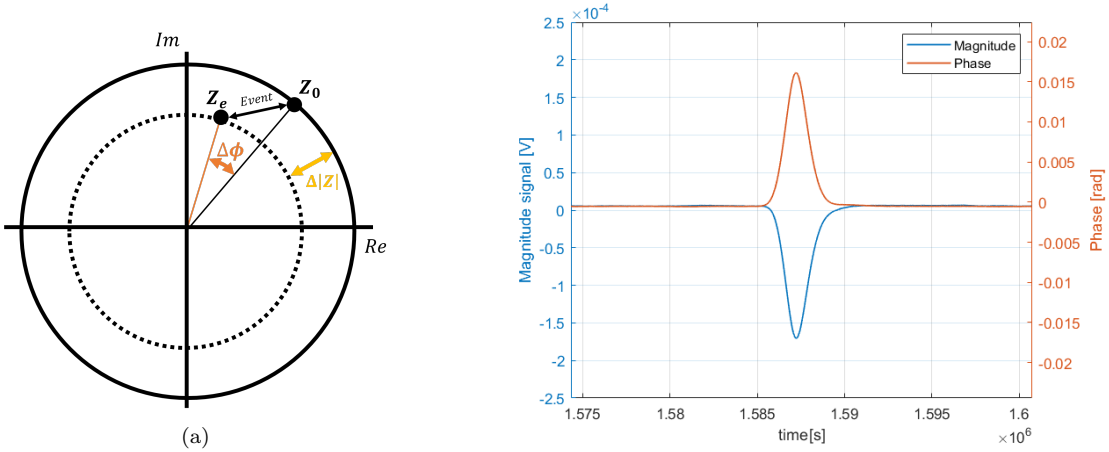

(a) (b)

Figure 5.2: **(a)** Visualization of an event. The change of the dot represents a change of the impedance Z **(b)** Event with normalized base signal

5.1.1 Influence of bead size

The primary ability of the impedance sensor should be the detection and classifications of differently sized particles. At low frequencies (<1MHz), cells and particles can be treated as non-conductive spheres as described in section 2.2. The impedance data at low frequencies is expected to provide the volume of a particle or cell. Figure 5.3a shows the a short segment of the baseline-compensated signal from an experiment where a mixture of 5,8 and 15 micrometer beads were combined in PBS and the impedance was measured with a frequency of 200kHz. All the peak magnitudes and transit times are combined in the scatter plot in figure 5.3b. A clear distinction between beads of different size can be made with solely the peak magnitude. Significant scattering in horizontal direction indicates a large range of transit times. The influence of bead velocity on the peak magnitude will be discussed later on. The variance in peak magnitude for each bead size corresponds with a positional dependence.

Figure 5.3c depicts the results of five experiments with different bead sized combined in a scatter plot. Although there is substantial scattering of events, the "cloud" of each bead size is relatively separated. Figure 5.3d shows how the events are distributed for each bead size.

To investigate the influence of bead material properties, polystyrene beads containing magnetite, and beads coated with COOH groups were measured in contrast with plain beads. No significant differences in the results were found, except that the COOH-coated beads were less prone to clogging. The reason why the magnetic beads behave similarly to normal beads may be due to the composition. A magnetite coating is located underneath an outer coating of polystyrene, which acts as an insulation layer.

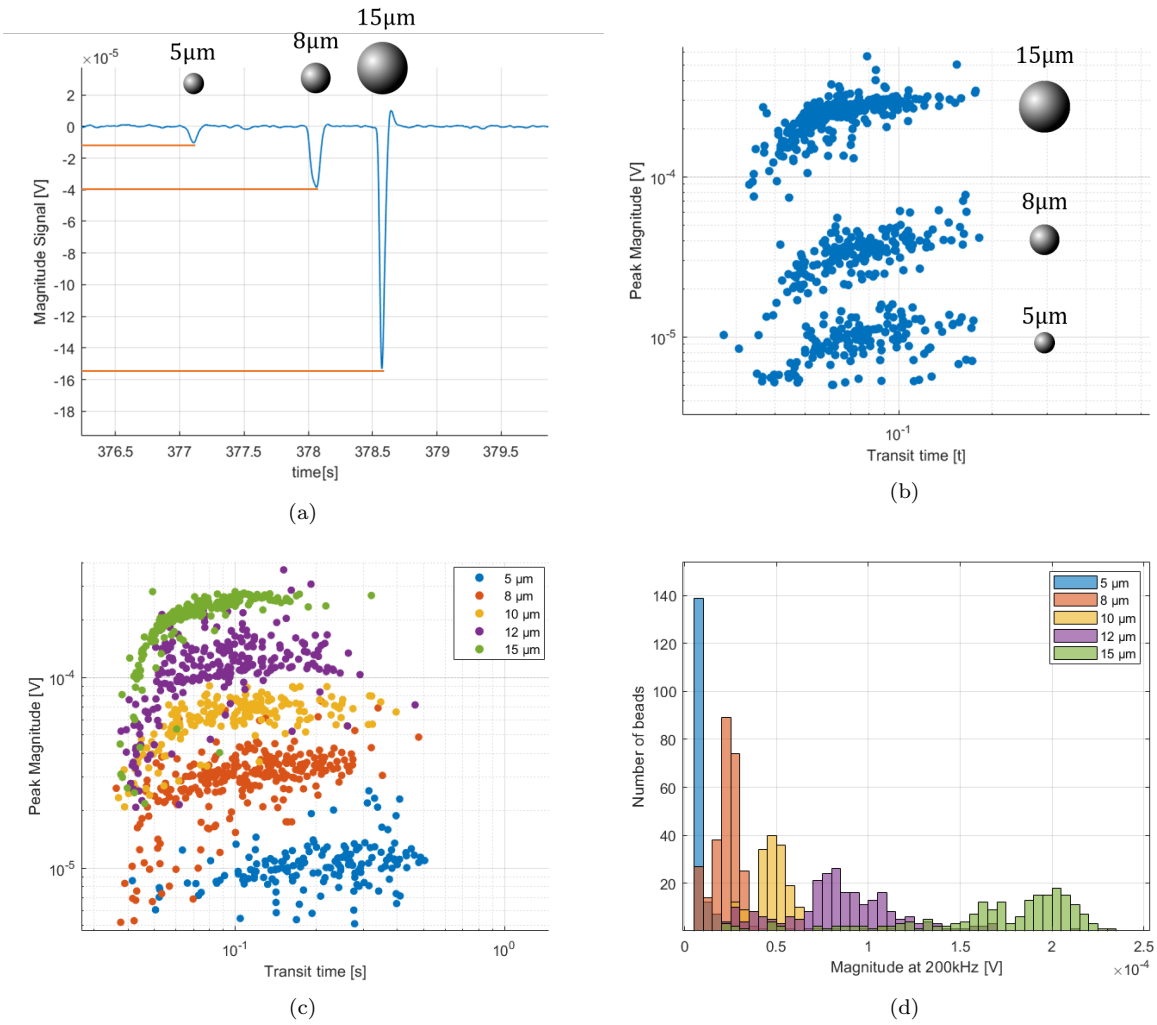

Figure 5.3: **(a)** Magnitude change as differently sized polystyrene beads flow through the electric field with a frequency of 200KHz and 1V. **(b)** shows the scatter plot of the diffently sized beads in a mixture. **(c)** Scatter plot of differently sized beads in separated experiments, but with the same device and conditions **(d)** Histogram showing the distribution of of peak magnitude for each particle size.

5.1.2 Influence of bead velocity

Besides affecting the width of the peak, the speed at which the particle passes the electrodes also shows a relationship with peak magnitude. Investigating figure 5.3b and figure 5.3c, the broad horizontal distribution of the scatter plot shape indicates a high variance in transit time. At short transit times, a significant drop in peak magnitude occurs. Accurate size detection at low transit times becomes inconspicuous. The overlap in data points reveal a bead velocity limit at which the sensor, with current parameters, has difficulty in detecting the size accurately. This could be ascribed to the choice of a lock-in sampling rate that is insufficient. This choice was made to reduce the size of data files. With an eye on future work focused on higher throughput, increasing the sampling rate of the lock-in amplifier is expected to solve this. Figure 5.4a and 5.4b show the correlation between the peak width and bead velocity verified with optical imaging.

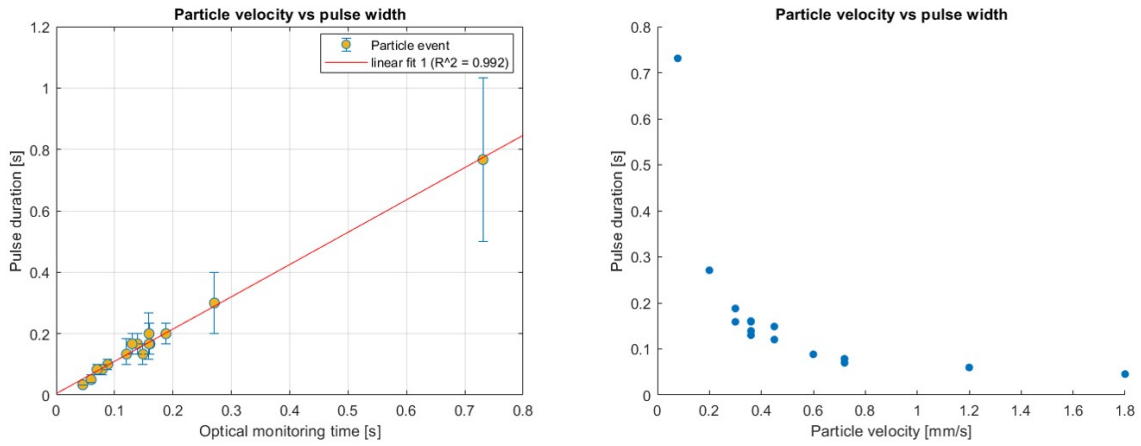

(a) (b)

Figure 5.4: **(a)** Electrical transit time correlated with the optical transit time. **(b)** Relation peak width with bead velocity

5.1.3 Influence of particle position

The electric field in coplanar configuration is not homogeneous, its stronger closer to the electrodes. The peak magnitude is dependent on the vertical particle position throughout the channel. To reduce the variance in particle position, the channel height is reduced as much as possible without obstructing flow of particles and causing channel clogging. Considering the scatter plot 5.3c, the variance in magnitude, i.e. the vertical scatter distribution at a given transit time correlates to the varying vertical position throughout the channel. Clearly, beads of 15 micrometer have a much lower vertical distribution compared to the smaller bead sizes, illustrating the interaction between particle diameter and channel height. A large bead has less space to move within the channel. The influence of bead velocity and position cannot be seen completely separate from each other. At lower flowrates, particles which have a slightly higher density than the medium, will sink to a lower positions in the channel and thus result in a higher impedance signal.

5.2 Device characterisation

The previous section the interaction between bead size, bead position and bead speed was investigated. This section will explore how the design parameters, such as channel geometry, electrode geometry and experimental conditions affect the sensitivity of the device.

5.2.1 Channel geometry

The sensitivity of the device is heavily dependent on the dimensions of the detection volume compared to the target particles. The simplest way to improve sensitivity is to decrease the detection volume. If the channel dimensions approach the diameter of the particles, the sensitivity is maximized but practical issues like clogging and dealing with tight fabrication tolerances arise. On the other hand, a larger channel cross section leads to a lower sensitivity and a higher chance of coincident particles in the detection area, increasing the amount of artefacts. The electric field is not homogeneous. Hence next to the volume fraction, the shape of the channel affects the sensitivity significantly. Figure 5.5a shows the correlation between sensitivity and channel width. It illustrates the increase in sensitivity through the impedance magnitude averaged over approximately 100 events as the channel width is decreased.

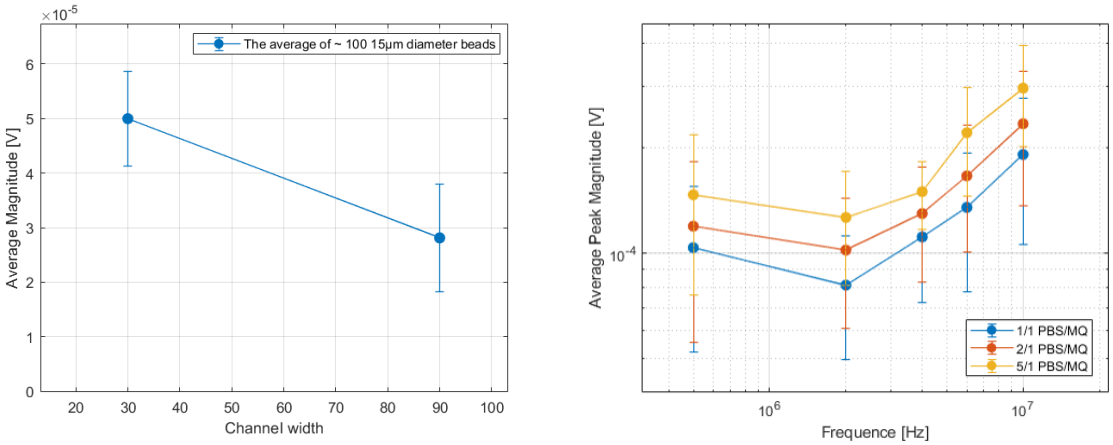

(a) (b)

Figure 5.5: **(a)** Increased sensitivity with channel width down-scaling. **(b)** The average magnitude versus frequency. Experiment with 15 micrometer beads in differential electrode configuration in a gradually increasing medium conductivity by changing the PBS/MilliQ ratio in 3 steps.

5.2.2 Medium properties

As expected, increasing the relative medium to bead conductivity would increase the sensitivity. Figure 5.5b shows the impact of a gradual conductivity increase on the average peak magnitude by a stewpise increase of the ratio PBS to purified water measured at different frequencies. When the medium conductivity was increased further by adding Sodium Chloride, electrode degradation due to chemical interaction at the electrode surface between the medium and the Chromium was brought about. Next to the conductivity, the medium density and osmolarity can be tuned with the addition of Sodium Chloride or sucrose [47] in order to match the density of particles or change cell properties with an osmotic shock.

5.2.3 Electrode geometry

The sensitivity is significantly impacted by the electrode spacing d_{el}, width w_{el} and thickness. The first parameter that is examined is the distance between the electrodes. The simulation in section 3.1 showed that with an increased electrode distance, the total signal variation would decrease, the width of the peak would increase and the signal would be less dependent on the vertical particle position.

Three devices were tested, where the d_{el} is varied from 20, 30 to 40 micrometer while the other design variables are constant. A mixture of PBS and 5,8, and 15 micrometer polystyrene beads were separately pumped through the devices. Figure 5.6a presents the experimental results of 15 micrometer beads passing the sensor in a peak magnitude versus peak width plot. In agreement with the simulations, the overall magnitude of the peak decreases with a larger d_{el}. The shape and density of the scatter clouds correlate to a varying flowrate and vertical particle position respectively. Interestingly, the scatter cloud of the smaller d_{el} show a steeper increase with bead velocity. This hints on a lower dependence of the peak magnitude on particle position and bead velocity for devices with a bigger gap between the electrodes, which would be in agreement with the simulations. The same trend is found in experiments with smaller beads, see figure 5.6b. As discussed before in section 3.2, the surface area of the electrodes interacts with the electric double layer at low frequencies. However, in practise there was no significant change when the electrode surface area was gradually increased with an increased w_{el} of 15, 20,25,30 to

50 μm.

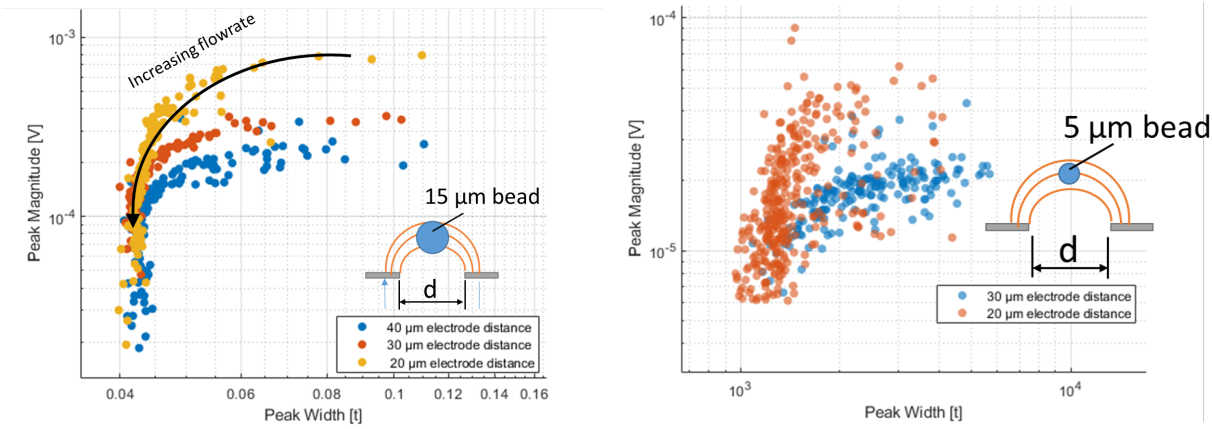

(a) (b)

Figure 5.6: **(a)** 15 μm beads in devices with varying electrode distances of 20, 30, 40 μm **(b)** 5 μm beads in devices with varying electrode distances of 20, 30 μm

In general there is a significant device-to-device performance variation. Underlying factors influencing the performance, could be the electrode surface roughness, small local differences in electrode thickness and local differences in channel geometry.

5.2.4 Absolute vs Differential electrode configuration

This section will reveal the trade-offs between the absolute and differential measurement configurations. Figure 5.7a compares the raw signal of the single electrode pair with the differential configuration.

Probing the impedance in single configuration brings about a volatile situation where fluctuations in baseline are caused by small changes in the device or by environmental electromagnetic pickup from other equipment. This complicates feature extraction and increases the chance of artifacts as a result of contaminated data. The advantage of the differential configuration is the measurement of cell properties directly against the surrounding media. By subtracting the signal of the reference pair from the pair in which the particles is located, baseline fluctuations caused by the environment are removed and the background and noise is reduced. This provides an improved sensitivity reflected by an increased signal to noise ratio. These improvements come with their own issues. Using three electrodes leads to a longer detection volume, which gives rise to a higher chance of coincident events, particularly at high flow speeds. Additionally, With differential measurements there are essentially two events per particle, making the post-processing procedure somewhat more complex.

For both methods, some drift of the signal is present. It occurs randomly and the reason is not completely understood. Compensation for this drift is necessary for extraction of relevant data as the fluctuations in baseline are significant compared to change in signal as a result of an event. By means of passing the raw signal through a moving average filter and subtracting it, the drift is removed. The result is a stable normalized baseline, from which event parameters can easily be extracted, see figure 5.7a. Applying the moving average filter results in some loss of information. An in depth signal conditioning analysis and an exploration of different methods for signal conditioning can be found in appendix E.

Figure 5.7b and 5.7c show scatter plots of experiments where beads of 5-,8 and 15 micrometer beads are measured in absolute and differential configuration. As expected, with the differential configuration the overall performance is improved. Less scattering in 5.7c, which is explained by a measurement that is more independent from environmental changes and thus more precise and accurate measurement of beads compared to 5.7b.

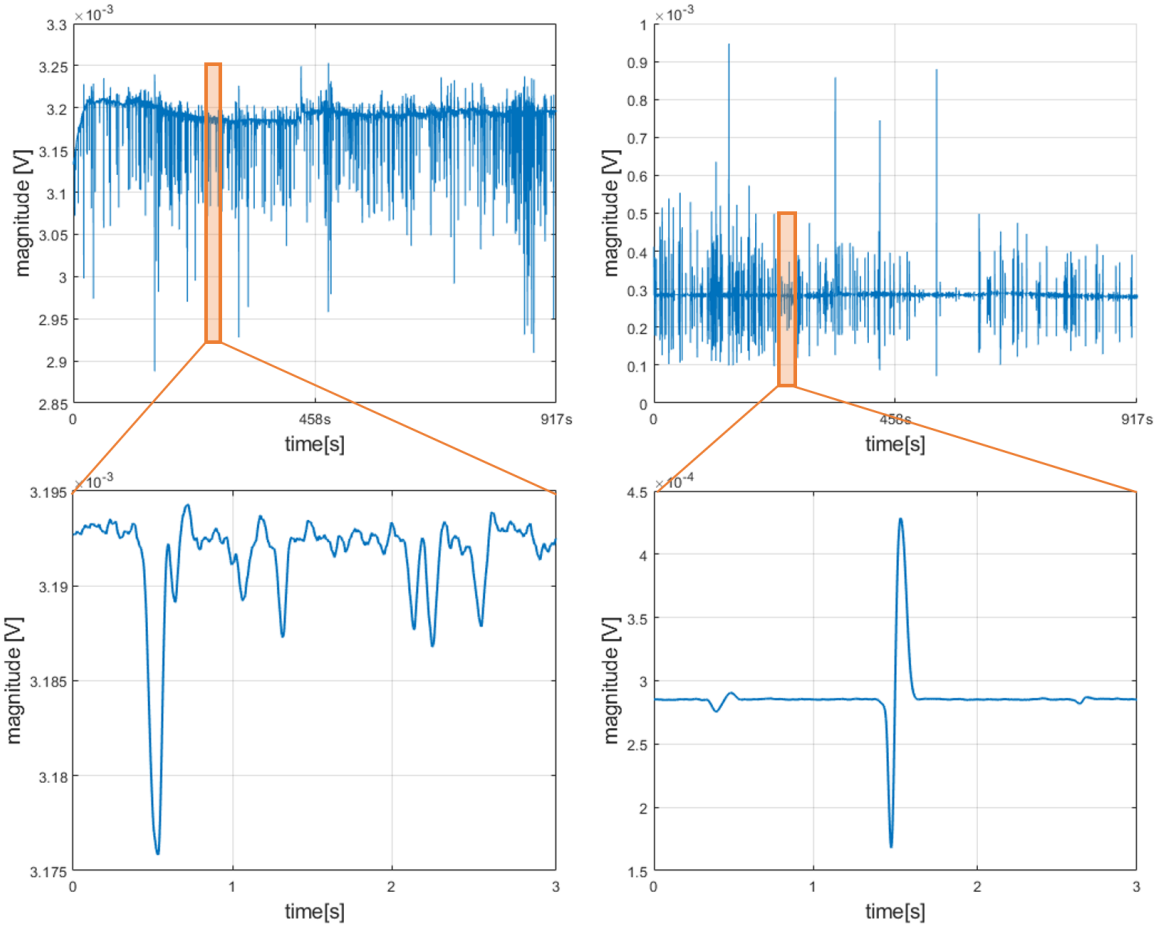

(a)

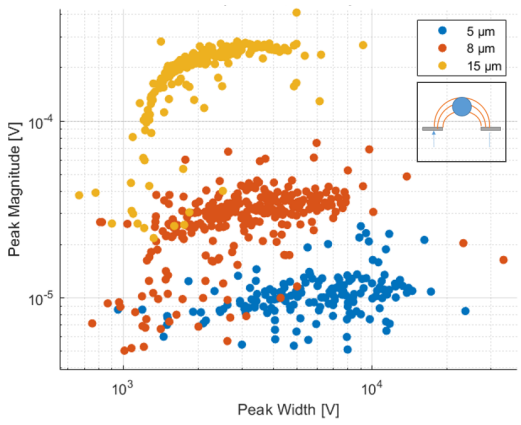

(b)

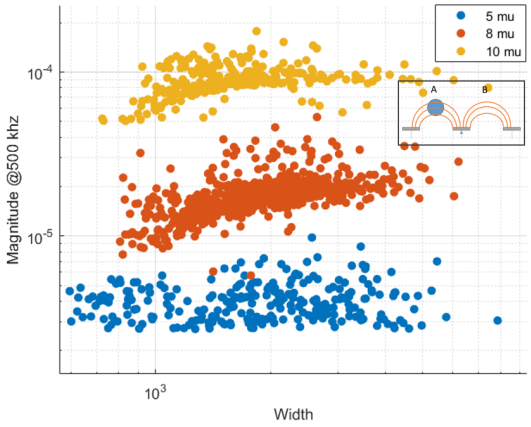

(c)

Figure 5.7: **a** comparison between **(left)** single electrode pair measurements (two electrodes) and **(right)**measurements in differential configuration (three electrodes) **(b)** Comparing scatter plots of single electrode pair and **(c)** differential configuration measurements

5.3 Spectral analysis

An essential step in device characterisation is the measurement of its behaviour as a function of frequency. Besides finding the optimal frequency for certain measurements, it exposes regions where noise and artefacts from the environment occur. The impedance spectrum can reveal underlying processes, for example the frequency regions where the electric double layer and parasitic capacitance dominate. Figure 5.8 displays the impedance spectrum of a single electrode pair device filled with only PBS, created by a EIS measurement with a potentiostat (Biologic SP-150). It shows the magnitude and phase of the impedance over frequency. Additional information regarding EIS experiments can be found in the appendix D.

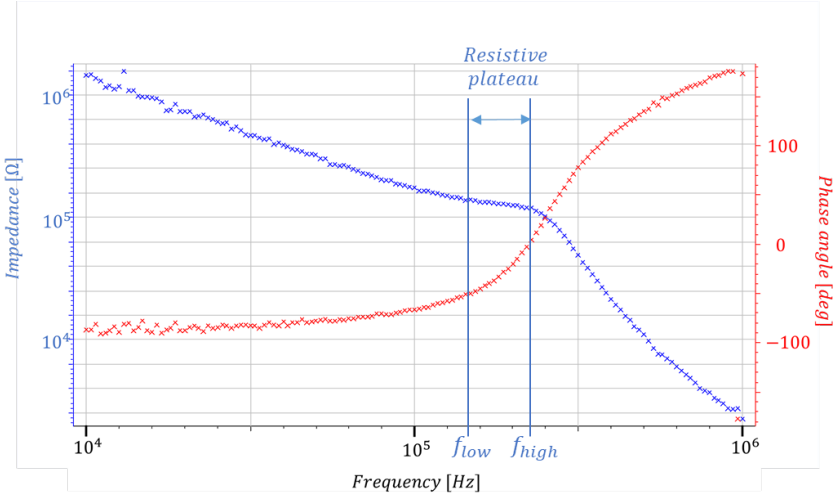

Figure 5.8: Electrochemical impedance spectrum measured with a Biologic SP-150 Potentiostat. 10 mV potential is applied as the frequency is step-wise increased up until 1MHz and the current response is measured. The resistive plateau

Figure 5.8 shows the three regions described in section 3.2 At low frequency, the impedance is high revealing the effect of the capacitive double layer at the electrodes. Around 200 kHz, the impedance of the double layer capacitance becomes lower than the impedance of the medium resistance. The magnitude stabilizes and transitions into a resistive plateau that continues to around 400 kHz. The resistive plateau indicates a frequency independent region, where the impedance correlates with the medium conductivity, and therefore permits unbiased impedance measurements. When increasing the frequency further, the impedance magnitude drops and the region where parasitic capacitive effects of the medium and electrical components dominate, is reached. The phase curve in figure 5.8 is not completely understood. It's expected that the maximum phase angle and the resistive plateau appear at around the same frequency. The phase angle is negative at low frequencies and becomes positive at the frequency of the plateau. A negative phase angle would indicate that the voltage lags the current, typical for capacitive effects. A positive phase means that the voltage leads the current, which is inductive behaviour.

The setup allows for simultaneous generation and measurement of six different frequencies, which makes it possible to extract an instantaneous spectral fingerprint of a single cell or particle that passes the electrodes. Figure 5.9a shows an event in differential mode measured at six different frequencies. This makes it possible to extract information regarding the spectral behaviour of a particle. Figure 5.9b depicts the spectrum of differently sized polystyrene beads by virtue of the magnitude signal averaged over 200 events over 6 different frequencies. It shows that particle size is dominant over the whole spectrum for polystyrene beads with a 5-, 8-, 10-, 12-, and 15 $-\mu m$

diameter. With this information a frequency can be chosen that exposes the size of a particle correctly, while also having a high SNR. Considering the plateau in figure 5.8 and the spectrum of figure 5.9b, 200 kHz and 500kHz are both suitable frequencies for size measurements.

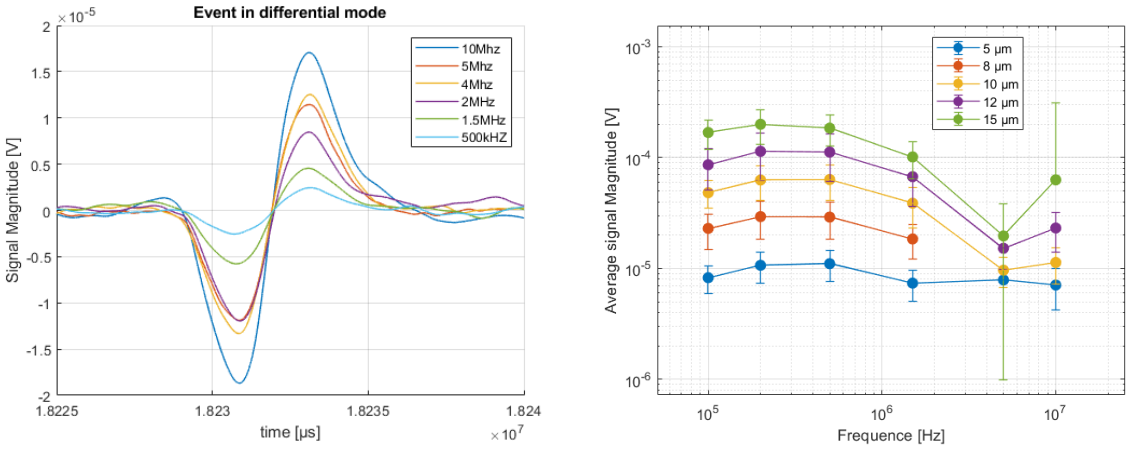

(a) (b)

Figure 5.9: **(a)** an event in differential configuration with six simultaneous frequencies. **(b)** the impedance magnitude mean of 200 particle events for each bead size and frequency measured with a single pair electrode.

5.4 Charactersing the dielectric properties of cancer cells

When instead of solely PBS, a particle suspended in PBS is positioned in the middle of the electric field and a frequency sweep is executed, it is possible to see the frequency dependent fingerprint of that particle. Placing a particle in the middle of two electrodes and keeping it there however is no easy feat, as the pressure at which it moves is very low. Figure 5.10a shows the percentage of change in magnitude that a particle causes which is located in the middle of 2 electrodes compared to the situation without a particle. The values of the magnitude heavily depend on the position of that particle in the channel. For that reason only the shape of the curve is relevant.

At low frequency, both the cell membrane and bead act as an insulator, where the magnitude change is mostly related to the volume. When studying the higher frequencies around 1 MHz, the difference between cells and beads can be revealed. The steeper drop in impedance magnitude for cells compared to polystyrene beads at around 1 MHz, which is the $\beta-$ dispersion region, suggests the effect of the effective short-circuiting of the membrane capacitance. When examining the averaged peak magnitudes over multiple frequencies of around 200 cancer cells and comparing them with polystyrene beads, depicted in figure 5.10b, a similar trend is revealed. These observations signify that in this frequency region the electric dipoles in the membrane can no longer follow the oscillations and current can start to pass trough, as discussed in section 2.2. This also resembles the trend of the cell simulation in section 3.3.

When investigating a further frequency increase, the impedance magnitude for particles and cells both drop at 5 MHz and rises again at 10 MHz. The drop at 5 MHz coincides with unusual peaks in the frequency sweeps, which could be device related, electromagnetic pickup from the equipment or noise from other sources. This can be seen in appendix F.2. This gives reason to believe that the impedance magnitude at 5MHz is artificially low.

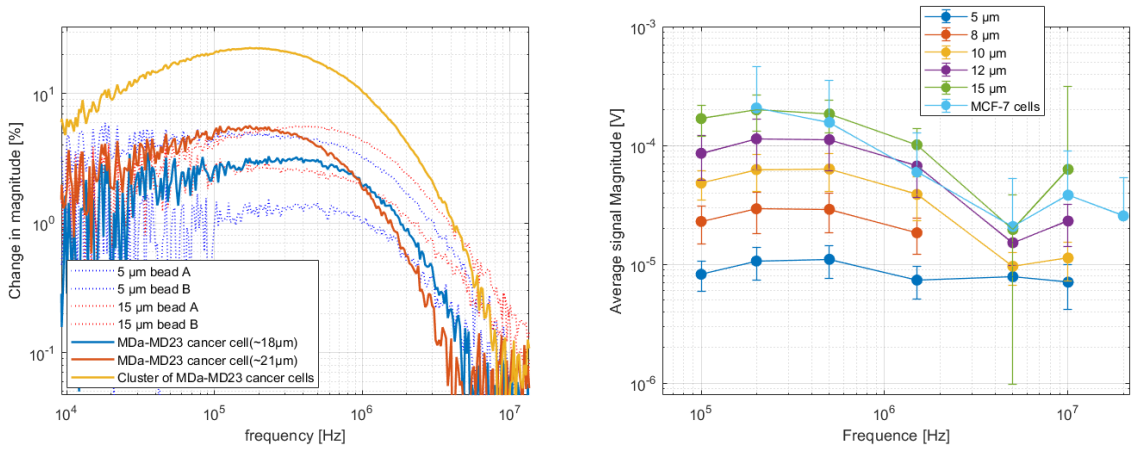

(a) (b)

Figure 5.10: **(a)** Frequency sweep where a cell or bead is located in the electric field. **(b)** Average impedance magnitude over different frequencies for each bead size compared to MCF-7 cells

Exploiting this difference in magnitude between low (<500 kHz) and intermediate (2-6 MHz) frequencies between cells and beads is a good strategy for cell discrimination. The ratio between intermediate and low frequency, the magnitude opacity [48, 31], is a very useful metric that carries information regarding cell membrane characteristics. Figures 5.11a and 5.11b adopt the opacity metric to differentiate between a mixture of differently sized polystyrene beads and a separate experiment with MCF-7 cancer cells. Figure 5.11a plots the low versus medium frequency impedance magnitude. The location of the cell cloud underneath the bead cloud indicates a lower opacity. The large spread of cell events with similar opacity indicate the large variation of cell sizes within the population. Figure 5.11b essentially contains the same information.

Figure 5.11c plots a mixture of 5 and 15 μm beads combined with MD cancer cells. Next to the peak width, peak magnitude and the opacity, the phase change is another property through which particles and cells can be discriminated. Particularly at high frequencies (10MHz), the distinction between particles and cells is apparent. Figure 5.11d plots the the impedance magnitude versus the phase. At this particular frequency, particles have a negative phase compared to a positive phase of the cells. Interestingly, there is a linear trend between the phase and magnitude for polystyrene beads. Comparing the phase and magnitude of a single particle facilitates differentiation. The phase, although harder to interpret, also contains useful information. Very recently, a study [33] introduced a phase-opacity metric ($\phi_{50MHz}/\phi_{500kHz}$) that correlates with the cell permittivity to conductivity ratio, revealing the dielectric behaviour of the cell interior. It showed that this phase metric scales inversely with interior cell conductivity.

To verify the results in the scatter plots, a part of the impedance data was labeled through optical imaging, see figure 5.12a. Additional cell experiments, where data was optically labeled and the reflection of light on the cell might indicate the vertical position in the channel can be found in the appendix F.3.

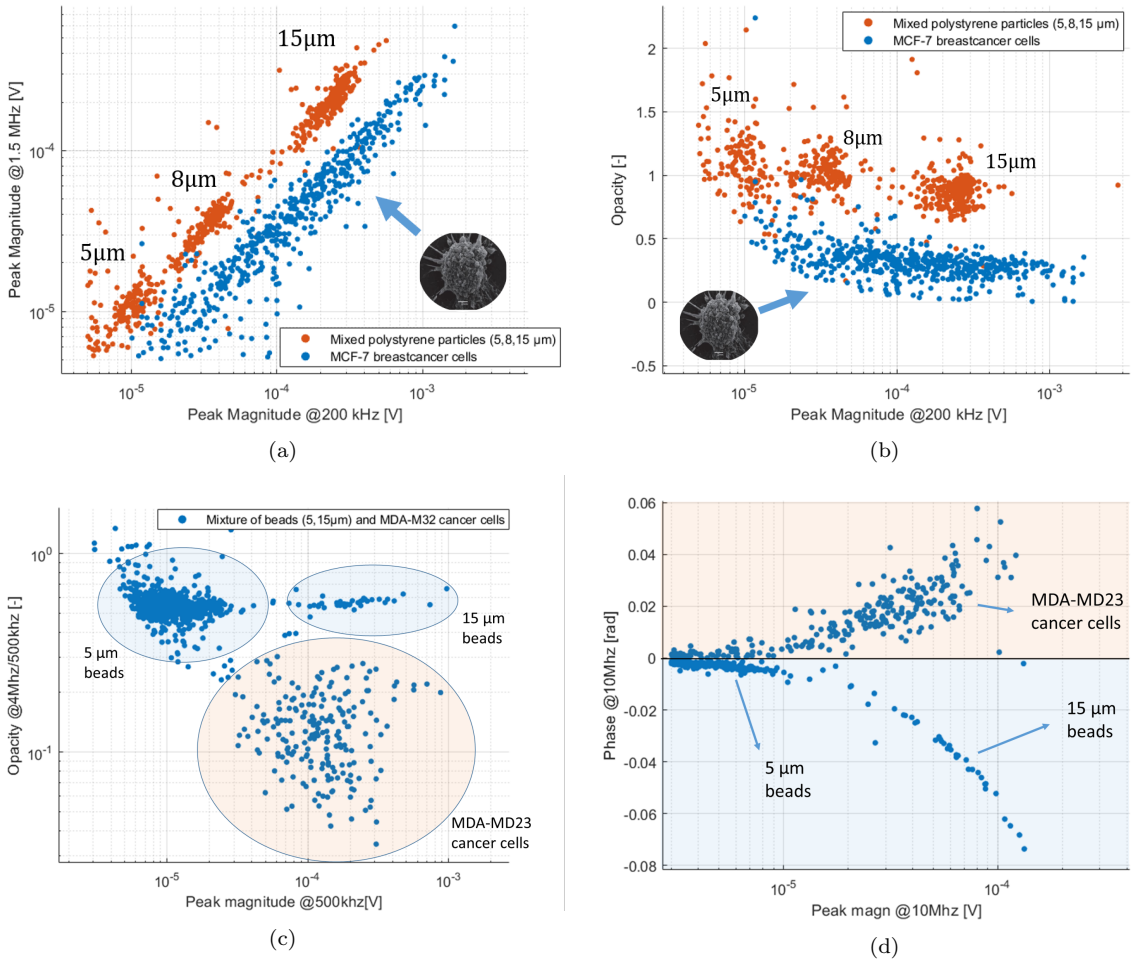

Figure 5.11: **(a)** Single pair electrode experiment. It plots of impedance magnitude at low versus intermediate frequency **(b)** Same experiment as on the right. It plots the low frequency impedance, indicating the cell size versus the opacity metric ($|Z|_{1.5M}/|Z|_{0.2M}$. **(c)** Experiment with a mixture of MDA-23 cancer cells and 5 and 15 μm beads in differential configuration. It plots the low frequency impedance on the x-axis, indicating the cell size versus the opacity metric ($|Z|_{6M}/|Z|_{0.5M}$. **(d)**Same experiment as on the left side. It plots the high frequency (10MHz) impedance versus magnitude versus the phase

5.4.1 MCF-7 versus MDA cancer cells

Discriminating cells from polystyrene beads is a fundamental first step. Characterizing dielectric properties of single cells within a population to distinguish healthy cells from cancer cells is less straight forward. In an attempt to differentiate between MDA-MD23 and MCF-7, these two cell populations were examined and compared. The physical differences between MDA-M23 and MCF-7 cancer cells are expected to be very small as they both are epithelial cancer cells. Using any of the aforementioned metrics was insufficiently sensitive for discrimination of these two cell populations. The scatter plots for both populations overlap with each other. However, by exclusively studying the in-phase component of the impedance, a slight distinction could be made. The in-phase component represents the real part of the impedance, i.e. correlating to the resistance. Figure 5.12b shows a plot where the amplitude of the in-phase components at 500 kHz and 6 MHz are compared. Because both cell population were measured in separate suspensions, to ensure comparability, 5 micrometer beads were added as reference. The high amount of scattering between both cell populations makes it hard to draw any conclusions. The

scattering is related to a heterogeneity in cell size and the fact that the cells when transferred from the growth medium to PBS, are accompanied with a substantial amount of undesirable debris. Solution can be found improving the centrifuge protocols to separate cells from debris in a better way.

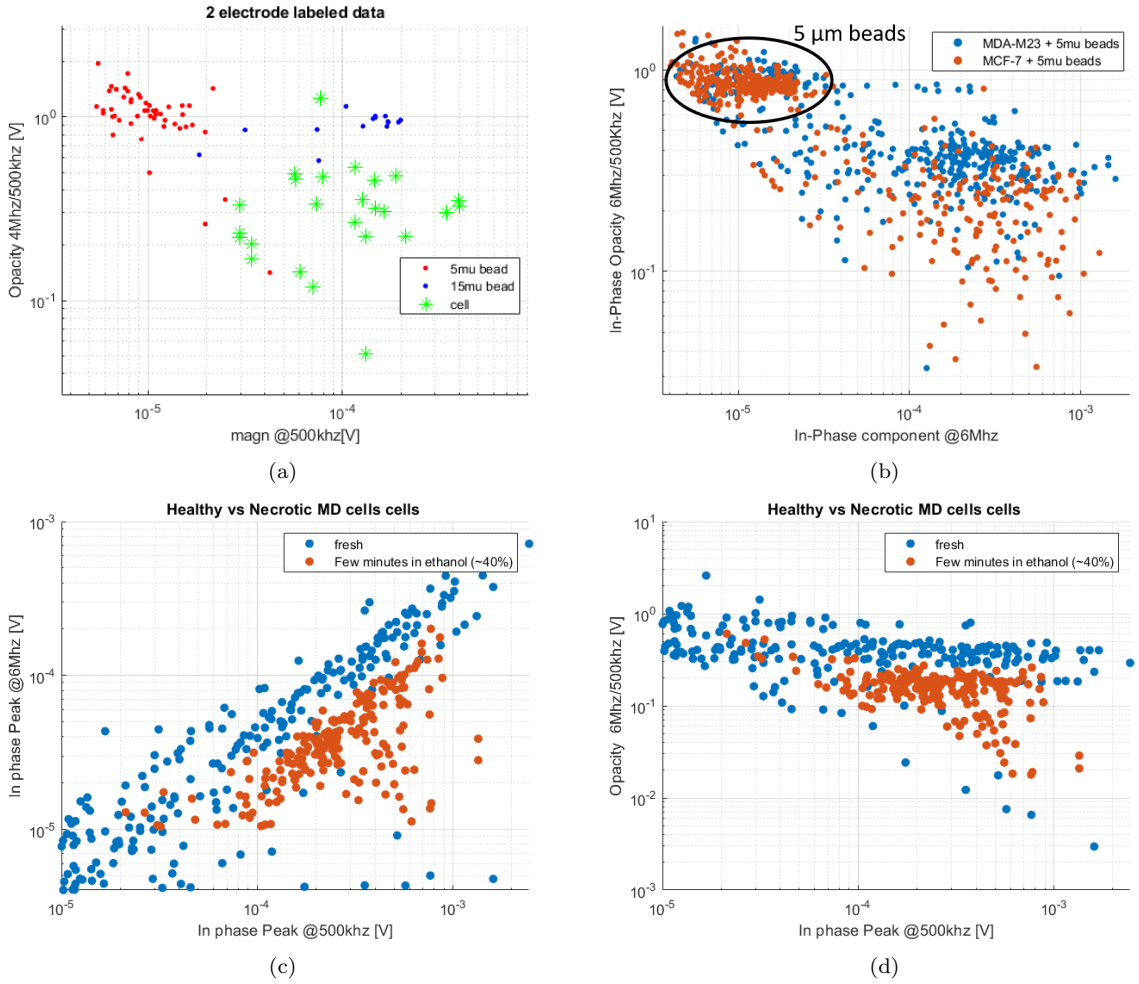

Figure 5.12: **(a)** verification of impedance data on a mixture of MDA-M23 cells and beads with a diameter of 5 and 15 μm.**(b)** comparison of MDA-23 and MCF-7 cancer cells **(c)** Experiment where fresh cells are compared versus cells which have been exposed to ethanol **(d)** Same as on the left side, but the opacity versus low impedance magnitude

5.4.2 Live versus necrotic cancer cells

To substantiate the influence of the membrane capacitance on the impedance data at intermediate frequencies, an experiment was conducted where the cell membranes were modified. This was achieved by necrosis, the injuring of cells with death as a result. This process is often accompanied with swelling and increased permeability with break-down of the plasma membrane integrity [49]. A population of MD cancer cells was separated into two batches. One of the batches was exposed to a solution with 40% ethanol for a few minutes, while the other was fresh. Subsequently both fresh and ethanol-exposed cells were measured with the impedance sensor in separate experiments. Figure 5.12c and 5.12d shows that with a combination of the in-phase amplitudes at 500 kHz and 6MHz a distinction between fresh and ethanol-exposed cells can be made. The ethanol-exposed cells shows a lower opacity, while having similar size indicated by the amplitude

at 500 kHz. This suggests that the ethanol-exposed cells exhibit a lower membrane capacitance compared to healthy fresh cells. However, to verify the results, the same experiment should be repeated with the addition of reference beads to calibrate both experiments.

5.5 Neural network classification

The amount of data extracted from the raw signals of 6 different frequencies is substantial. Upon cell passage, for each separate frequency a certain change in magnitude and phase occurs, both producing a peak magnitude and peak width. This condensates down to the extraction of 4 parameters per event per frequency, with a total of 24 parameters. These parameters can also be used to calculate magnitude opacity metrics, a combination of the peak magnitude at different frequencies, producing an additional 15 metrics. In total this adds up to 39 parameters. Doing the same with the separate in- and out-of phase signals, produces an additional 39 parameters. Parameters extracted from the in- and out-of-phase components contain information identical to the parameters from the magnitude and phase. However, certain characteristics may only be exposed through either the Cartesian or polar signal format. Any combinations of the total of 78 parameters can be plotted in 2D or 3D, revealing certain characteristic of a sub-population. The plots carry information regarding the properties of cells and particles and can be useful for population differentiation. However, investigating all possible combinations is time-consuming and the exact meaning of this information is hard to pin down. In the previous sections, it is shown that low frequency measurements exhibit information regarding the cell size and the ratio of low to intermediate frequency discloses information on the dielectric properties of the cell membrane. Figure 5.13 shows a selection of possible plots of an experiment with a mixture of beads (5 and 15 micrometer) and MD cancer cells to exemplify the many ways of differentiation.

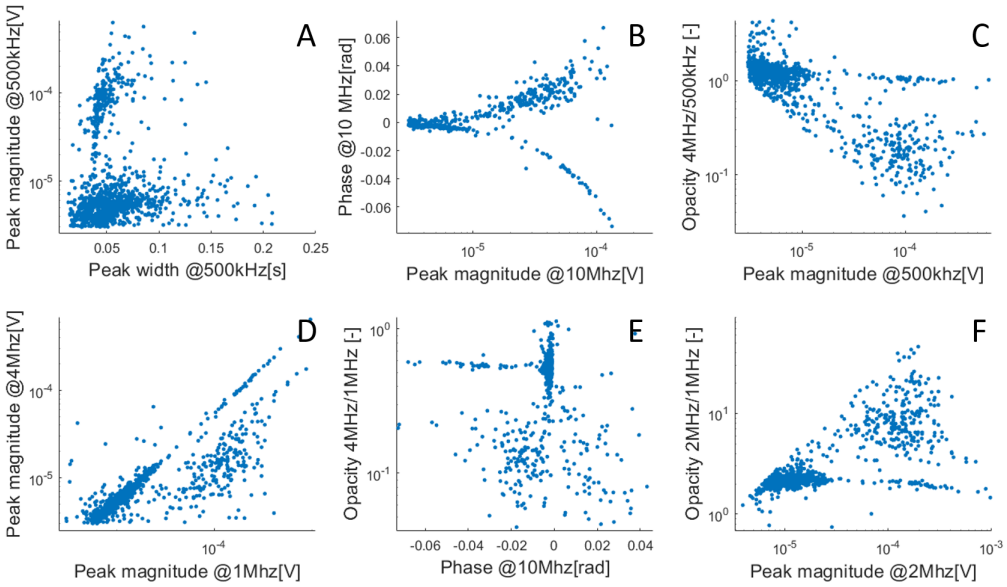

Figure 5.13: a selection of plots with different variables extracted from an experiment with a mixture of beads (5 and 15 micrometer) and MD cancer cells. Note that the amount of 15 micrometer beads in the mixture was much smaller than the amount of 5 micrometer beads and cancer cells.

Previously, a multitude of properties measured with the microfluidic impedance chip to distinguish cells were introduced. The raw signals were converted into relevant data. The many variables

form a large data set that contains a high degree of ambiguity. This section will discuss the classification of this impedance data with the application of machine learning techniques. Theory, background and the full scripts of the algorithms can be found in the appendix.

The final application, out of the scope of this particular work, will be in hardware based neural networks. Obstacles arise with the transition from digital software neural networks to analogue hardware- based neural networks, where the weights and biases are programmed in an analogue fashion. To ease the transition, the software neural network algorithm should be as simple as possible. For this reason a simple and elegant perceptron algorithm will be trained to classify three sizes of polystyrene beads. This network uses two inputs, the transit time and peak magnitude at 200KHz and will create two output boundaries to separate the three categories. The weights are changed in order to translate and rotate the boundary line. The training data set consists of a total of 1151 labelled events. Figure 5.14 shows the two output boundaries after training. Due to the scatter clouds being almost fully separated, classification of the size categories is straightforward. The only error is a result of data points located in the incorrect region.

Showcasing the capability of software neural networks, a more ambiguous data set with significant overlap in combination with a more elaborate neural network is used to distinguish between healthy and necrotic cancer cells. A two-layer feed-forward network with a hidden layer, consisting of 10 neurons with a Sigmoid transfer functions. The two output neurons consist of a softmax transfer function. The algorithm will be trained with scaled conjugate gradient back-propagation using the MATLAB neural network pattern recognition application. The complete data-set, consisting of the peak magnitudes, peak widths and opacity at frequencies at 500 kHz and 6 MHz was randomly divided into three groups. The largest part, 70%, for training and the rest assigned for validation data (15%) and testing data (15%). The result was a combined success rate of 88.9 %. Additional information regarding the results, like the ROC curve **??** illustrating the quality of the classifiers can be found in the appendix B.1.

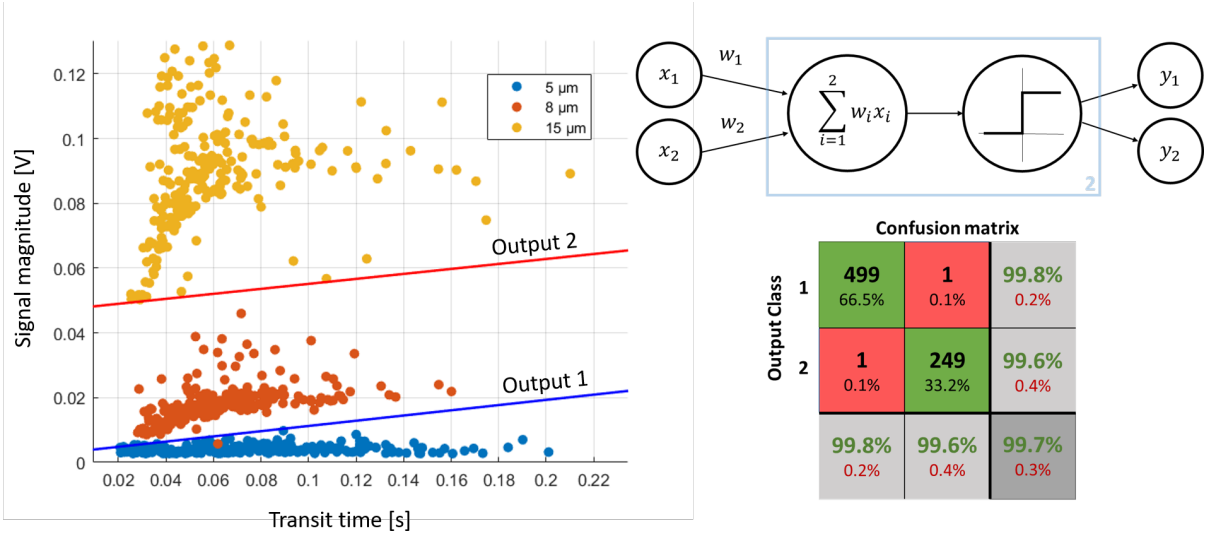

Figure 5.14: a selection of plots with different variables extracted from an experiment with a mixture of beads (5 and 15 micrometer) and MD cancer cells. Note that the amount of 15 micrometer beads in the mixture was much smaller than the amount of 5 micrometer beads and cancer cells.

6 Conclusion & outlook

6.1 Conclusion

The objective of this thesis was to develop a simple microfluidic impedance sensor capable of detecting and distinguishing label-free cancer cells to provide a neural network with useful data on dielectric cell characteristics. To achieve this, an impedance sensor in the form of a microfluidic channel with coplanar integrated electrodes was designed and fabricated. It simultaneously measures the impedance for each particle at six frequencies from which the magnitude, phase and opacity data can be used to distinguish beads and cells, effectively characterizing the size, transit time and dielectric properties.

The impedance measurements at low frequency successfully probe the particle size, as demonstrated with the differentiation of polystyrene beads with varying size. Although there still is a dependence on particle position responsible for some variance, by downscaling the channel and increasing the electrode distance, this dependence was reduced. By directly measuring the cell properties against the surrounding media in differential mode, environmental influences and noise were reduced, which ultimately improved the sensitivity.

The sensor was used to examine the dielectric properties of cancer cells. Investigating the spectral behaviour of cells, a larger decrease in impedance magnitude was found for cells compared to beads at intermediate (1MHz) frequency levels. This correlates with the decrease in polarization of the cell membrane capacitance. By probing simultaneously the low (200-500kHz) and intermediate (1-5 MHz) frequency impedance magnitude, i.e. the opacity, dielectric information regarding the membrane capacitance was obtained. This was demonstrated by differentiating between live cancer cells and those with compromised membranes.

The capability of the sensor to offer multiparametric information that conveys cell velocity, cell size and its dielectric properties makes it ideal for neural network implementation. The data extracted from the sensor was used to train a simple software-based perceptron neural network to classify differently sized beads, paving the way for future application of hardware-based neural networks.

6.2 Outlook

Various aspects of the impedance sensor can be improved upon. Nevertheless, this work is a good starting point for future work.

As this project was the first exploration of impedance cytometry, there was no particular focus on high throughput. With current measurement parameters, high bead velocity reduces the ability of the sensor to accurately measure the size and dielectric properties. This is most likely caused by the low sampling rate of the lock-in amplifier and can easily be tested by increasing the sampling rate in future experiments.

Regarding the setup, there is much room for improvement. The current noise and drift in the signal are partly a result of electromagnetic pickup from the environment. By creating a robust chip-holder, improving the connection between cabling and device, or electrically shielding the device, environmental influences could be reduced leading to a higher sensitivity.

This work centered around lower and intermediate frequency regions. The current setup allows for the measurement of much higher frequency regions up to 50MHz, which could provide other cell characteristics such as the dielectric properties of the cytoplasm and nucleus. Additionally, the change in phase could be further exploited, as it contains useful dielectric cell information.

Although the sensor produces plenty of data, extracting relevant information and coupling it to specific cell components is difficult. To create a better understanding of what the experimental impedance data means, additional modelling would be beneficial. Specifically, the further use of the Maxwell's mixture theory, equivalent circuits and multi-shell models to compute cell dielectric properties by fitting experimental data to simulated models would provide new insights.

Future work revolves around the combination of impedance sensing with other physical sensors to provide input for a hardware-based neural network. Each physical sensor in the chip should target other cell characteristics in a label-free way. Impedance cytometry, next to providing metrics regarding dielectric properties, can also provide information regarding morphology[50]. A logical next step would be the integration of a constriction channel into the impedance sensor. This is an elegant way of combining electrical- with mechanical- sensing [51, 52, 53] in a single channel providing a unique set of intrinsic cell characteristics. Combining impedance cytometry with electrical impedance spectroscopy (EIS) could provide useful information [54] as well. A suitable first candidate based on a completely different method would be optical sensing. The integration of a laser and a photo-detector in a channel, next to the impedance sensor, could prove to be very effective [55].

The translation of analogue output signals to useful data needs to be integrated into the chip. For this reason, the threshold-based data extraction method in this project was kept simple. This eases the transition from software data extraction to the extraction of relevant data by hardware components. Future work includes the investigation of possible hardware-based components that extract the peaks from the analogue signal.

Considering lab-on-a-chip applicability, i.e. integration of all components of the setup into a modular platform, the main predicament is created by the lock-in amplifier. It may be a powerful and versatile part of measuring equipment, but at the same time it's bulky and expensive. Shrinking this component could be achieved with custom-designed electronics. To scale down the footprint of Lock-in amplification equipment, Talukder et al.[56] developed a wireless handheld lock-in amplifier capable of single low-frequency impedance measurements. Additionally, it could perform baseline drift substractions to improve the SNR. Dekker et. al [57] developed a modular microfluidic chip where detection was done with a direct digital synthesis (DDS) integrated circuit that generates the signal. The lock-in process and detection of signal changes are performed by an analog to digital converter (ADC) in combination with a digital signal processor. To reduce cost, simple impedance cytometers can be integrated into custom printed circuit boards (PCB) [58]. Other solutions to get around the powerful yet bulky lock-in amplifiers, might be found in CMOS based impedance sensing [59]. Carminati et. al [60] developed an impedance cytometer with a CMOS lock-in demodulator and a delta-sigma analogue to digital converter.

7 Acknowledgements / Dankwoord

Nine months I started this project. I probably never expected the final chapter of my study would end with a "doorhaaldonderdag". This time instead of doing the things related to a classic doorhaaldonderag, it was a night of blood, sweat and copious amounts of grammar. I am keeping it short, as the deadline approaches. Looking back, first I want to thank my supervisors Yoeri and Eveline for their guidance (and the free coffee). Thanks goes out to Jaap den Toonder and Arjen Frijns for being part of my defense committee. I also want to thank everyone else in the lab who helped me around, or whom I had great conversations with around the coffee machine. Special thanks to people who kept me company in the "schuilkelder" from start to finsish. Additionally, I want to thank everyone who took the time to proofread my thesis. This made it much better.

The completion of my study would not have been possible without my friends, especially, the boys from the south and "die mensen van Integrand" who are probably waiting for a good quote like "Use what talents you possess - the woods will be very silent if no birds sang there except those that sang best." -Henry van Dyke. Or a personal favorite: "They Don't Think It Be Like It Is But It Do" by Oscar Gamble.

Last but not least, most special thanks to my family for their unconditional love and support throughout the years.

Bibliography

[1] Chang Yang et al. "Circulating tumor cells in precision oncology: clinical applications in liquid biopsy and 3D organoid model". In: *Cancer Cell International* 19.1 (2019), p. 341.

[2] Mi-Young Kim et al. "Tumor self-seeding by circulating cancer cells". In: *Cell* 139.7 (2009), pp. 1315–1326.

[3] André A Adams et al. "Highly efficient circulating tumor cell isolation from whole blood and label-free enumeration using polymer-based microfluidics with an integrated conductivity sensor". In: *Journal of the American Chemical Society* 130.27 (2008), pp. 8633–8641.

[4] Francois-Clement Bidard et al. "Translating metastasis-related biomarkers to the clinic—progress and pitfalls". In: *Nature reviews Clinical oncology* 10.3 (2013), pp. 169–179.

[5] Thore Hillig et al. "In vitro validation of an ultra-sensitive scanning fluorescence microscope for analysis of Circulating Tumor Cells". In: *Apmis* 122.6 (2014), pp. 545–551.

[6] W Jeffrey Allard et al. "Tumor cells circulate in the peripheral blood of all major carcinomas but not in healthy subjects or patients with nonmalignant diseases". In: *Clinical cancer research* 10.20 (2004), pp. 6897–6904.

[7] Ki-Ho Han, Arum Han, and A Bruno Frazier. "Microsystems for isolation and electrophysiological analysis of breast cancer cells from blood". In: *Biosensors and bioelectronics* 21.10 (2006), pp. 1907–1914.

[8] Jaap den Toonder. "Circulating tumor cells: the Grand Challenge". In: *Lab on a Chip* 11.3 (2011), pp. 375–377.

[9] Daniel R Gossett et al. "Label-free cell separation and sorting in microfluidic systems". In: *Analytical and bioanalytical chemistry* 397.8 (2010), pp. 3249–3267.

[10] Peter RC Gascoyne et al. "Correlations between the dielectric properties and exterior morphology of cells revealed by dielectrophoretic field-flow fractionation". In: *Electrophoresis* 34.7 (2013), pp. 1042–1050.

[11] Carlos Honrado et al. "Single-cell microfluidic impedance cytometry: from raw signals to cell phenotypes using data analytics". In: *Lab on a Chip* (2021).

[12] Tao Sun and Hywel Morgan. "Single-cell microfluidic impedance cytometry: a review". In: *Microfluidics and Nanofluidics* 8.4 (2010), pp. 423–443.

[13] Christopher E Sims and Nancy L Allbritton. "Analysis of single mammalian cells on-chip". In: *Lab on a Chip* 7.4 (2007), pp. 423–440.

[14] James R Heath, Antoni Ribas, and Paul S Mischel. "Single-cell analysis tools for drug discovery and development". In: *Nature reviews Drug discovery* 15.3 (2016), p. 204.

[15] George M Whitesides. "The origins and the future of microfluidics". In: *nature* 442.7101 (2006), pp. 368–373.

[16] Shady Gawad et al. "Dielectric spectroscopy in a micromachined flow cytometer: theoretical and practical considerations". In: *Lab on a Chip* 4.3 (2004), pp. 241–251.

[17] Tao Sun and Hywel Morgan. "Single-cell microfluidic impedance cytometry: a review". In: *Microfluidics and Nanofluidics* 8.4 (2010), pp. 423–443.

[18] Hongyan Liang et al. "Characterization of Single-Nucleus Electrical Properties by Microfluidic Constriction Channel". In: *Micromachines* 10.11 (2019), p. 740.

[19] Daniel Spencer, Veronica Hollis, and Hywel Morgan. "Microfluidic impedance cytometry of tumour cells in blood". In: *Biomicrofluidics* 8.6 (2014), p. 064124.

[20] Yang Zhao et al. "Development of microfluidic impedance cytometry enabling the quantification of specific membrane capacitance and cytoplasm conductivity from 100,000 single cells". In: *Biosensors and Bioelectronics* 111 (2018), pp. 138–143.

[21] Yi Zhang et al. “Crossing constriction channel-based microfluidic cytometry capable of electrically phenotyping large populations of single cells”. In: *Analyst* 144.3 (2019), pp. 1008–1015.

[22] Rasool Fakoor et al. “Using deep learning to enhance cancer diagnosis and classification”. In: *Proceedings of the international conference on machine learning*. Vol. 28. ACM New York, USA. 2013.

[23] Andre Esteva et al. “Dermatologist-level classification of skin cancer with deep neural networks”. In: *nature* 542.7639 (2017), pp. 115–118.

[24] Alanna Vial et al. “The role of deep learning and radiomic feature extraction in cancer-specific predictive modelling: a review”. In: *Translational Cancer Research* 7.3 (2018), pp. 803–16.

[25] Steve Furber. “Large-scale neuromorphic computing systems”. In: *Journal of Neural Engineering* 13 (2016).

[26] Yoeri van de Burgt et al. “A non-volatile organic electrochemical device as a low-voltage artificial synapse for neuromorphic computing”. In: *Nature materials* 16.4 (2017), pp. 414–418.

[27] Luca Callegaro. *Electrical impedance: principles, measurement, and applications*. CRC Press, 2012.

[28] 16 Apr. 2021 Encyclopedia Britannica. *Dielectric*. URL: `https://www.britannica.com/science/dielectric`. (Accessed 20 May 2021).

[29] H Pauly and HP Schwan. “The impedance of a suspension of spherical particles surrounded by a shell”. In: *Z. Naturforsch* 14 (1959), pp. 125–131.

[30] Herman P Schwan. “Electrical properties of tissue and cell suspensions”. In: *Advances in biological and medical physics*. Vol. 5. Elsevier, 1957, pp. 147–209.

[31] Karen Cheung, Shady Gawad, and Philippe Renaud. “Impedance spectroscopy flow cytometry: On-chip label-free cell differentiation”. In: *Cytometry Part A* 65.2 (2005), pp. 124–132.

[32] Tzu-Keng Chiu et al. “A low-sample-loss microfluidic system for the quantification of size-independent cellular electrical property—Its demonstration for the identification and characterization of circulating tumour cells (CTCs)”. In: *Sensors and Actuators B: Chemical* 246 (2017), pp. 29–37.

[33] JS McGrath et al. “Electrophysiology-based stratification of pancreatic tumorigenicity by label-free single-cell impedance cytometry”. In: *Analytica chimica acta* 1101 (2020), pp. 90–98.

[34] Frederick F Becker et al. “Separation of human breast cancer cells from blood by differential dielectric affinity”. In: *Proceedings of the National Academy of Sciences* 92.3 (1995), pp. 860–864.

[35] A Zimmermann. “Nucleus, Nuclear Structure, and Nuclear Functional Changes in Liver Cancer”. In: *Tumors and Tumor-Like Lesions of the Hepatobiliary Tract* (2017), pp. 3043–3069.

[36] Jill A Gallaher, Joel Brown, and Alexander RA Anderson. “The dynamic tumor ecosystem: how cell turnover and trade-offs affect cancer evolution”. In: *BioRxiv* (2018), p. 270900.

[37] James Clerk Maxwell. *Preface to the First Edition, A Treatise on Electricity and Magnetism, Vol. 1*. 1954.

[38] James Clerk MAXWELL. “MAXWELL, James Clerk. A treatise on electricity and magnetism. Vol. I. Oxford: Clarenton Press Series, 1873. Preface, pV-XIV.” In: (1873).

[39] Tao Sun, Catia Bernabini, and Hywel Morgan. “Single-colloidal particle impedance spectroscopy: Complete equivalent circuit analysis of polyelectrolyte microcapsules”. In: *Langmuir* 26.6 (2010), pp. 3821–3828.

[40] Koji Asami. "Dielectric dispersion in biological cells of complex geometry simulated by the three-dimensional finite difference method". In: *Journal of Physics D: Applied Physics* 39.3 (2006), p. 492.

[41] Kenneth R Foster, Herman P Schwan, et al. "Dielectric properties of tissues". In: *CRC handbook of biological effects of electromagnetic fields* (1986), pp. 27–96.

[42] Jongin Hong et al. "AC frequency characteristics of coplanar impedance sensors as design parameters". In: *Lab on a Chip* 5.3 (2005), pp. 270–279.

[43] David Holmes et al. "Leukocyte analysis and differentiation using high speed microfluidic single cell impedance cytometry". In: *Lab on a Chip* 9.20 (2009), pp. 2881–2889.

[44] Jun Yang et al. "Differential analysis of human leukocytes by dielectrophoretic field-flow-fractionation". In: *Biophysical journal* 78.5 (2000), pp. 2680–2689.

[45] Medicago AB. *Phosphate Buffered Saline (PBS), pH 7.4 and 7.2*. URL: `http://www.medicago.se/sites/default/files/pdf/productsheets/PBS_Buffer_v._01.pdf`. (accessed: 01.01.2021).

[46] Micromod. *Micromer polystyren beads*. URL: `https://www.micromod.de/en/produkte-34-white_psm_cooh.html`. (accessed: 01.01.2021).

[47] Melanie Ostermann et al. "Label-free impedance flow cytometry for nanotoxicity screening". In: *Scientific Reports* 10.1 (2020), pp. 1–14.

[48] RA Hoffman, TS Johnson, and WB Britt. "Flow cytometric electronic direct current volume and radiofrequency impedance measurements of single cells and particles". In: *Cytometry: The Journal of the International Society for Analytical Cytology* 1.6 (1981), pp. 377–384.

[49] Adele De Ninno et al. "High-throughput label-free characterization of viable, necrotic and apoptotic human lymphoma cells in a coplanar-electrode microfluidic impedance chip". In: *Biosensors and Bioelectronics* 150 (2020), p. 111887.

[50] B De Wagenaar et al. "Towards microfluidic sperm refinement: impedance-based analysis and sorting of sperm cells". In: *Lab on a Chip* 16.8 (2016), pp. 1514–1522.

[51] Yi Zheng et al. "Electrical measurement of red blood cell deformability on a microfluidic device". In: *Lab on a Chip* 13.16 (2013), pp. 3275–3283.

[52] Ying Zhou et al. "Characterizing deformability and electrical impedance of cancer cells in a microfluidic device". In: *Analytical chemistry* 90.1 (2018), pp. 912–919.

[53] Xiang Ren et al. "Biophysical phenotyping of cells via impedance spectroscopy in parallel cyclic deformability channels". In: *Biomicrofluidics* 13.4 (2019), p. 044103.

[54] Yongxiang Feng et al. "A microfluidic device integrating impedance flow cytometry and electric impedance spectroscopy for high-efficiency single-cell electrical property measurement". In: *Analytical chemistry* 91.23 (2019), pp. 15204–15212.

[55] Allison Schaap, Thomas Rohrlack, and Yves Bellouard. "Optical classification of algae species with a glass lab-on-a-chip". In: *Lab on a Chip* 12.8 (2012), pp. 1527–1532.

[56] Niloy Talukder et al. "A portable battery powered microfluidic impedance cytometer with smartphone readout: towards personal health monitoring". In: *Biomedical microdevices* 19.2 (2017), p. 36.

[57] Stefan Dekker et al. "From chip-in-a-lab to lab-on-a-chip: a portable Coulter counter using a modular platform". In: *Microsystems & nanoengineering* 4.1 (2018), pp. 1–8.

[58] Yusheng Fu, Qingbo Yuan, and Jinhong Guo. "Lab-on-PCB-based micro-cytometer for circulating tumor cells detection and enumeration". In: *Microfluidics and Nanofluidics* 21.2 (2017), p. 20.

[59] Ava Hedayatipour, Shaghayegh Aslanzadeh, and Nicole McFarlane. "CMOS based whole cell impedance sensing: Challenges and future outlook". In: *Biosensors and Bioelectronics* 143 (2019), p. 111600.

[60] Marco Carminati et al. “Miniaturized impedance flow cytometer: Design rules and integrated readout”. In: *IEEE transactions on biomedical circuits and systems* 11.6 (2017), pp. 1438–1449.
[61] M. Hagan, H. Demuth, and M. Beale. “Neural network design”. In: 1995.

A The maxwell mixture theory

The electrical behaviour of a mixture of particles and electrolyte solution in a homogeneous electric field can be approached with Maxwell's mixture theory. [37, 38] This theory links the complex permittivity of the bulk suspension to that of the particle and suspending medium:

$$\tilde{\varepsilon}_{mix} = \tilde{\varepsilon}_{med}\frac{1 + 2\Phi\tilde{f}_{CM}}{1 - \Phi\tilde{f}_{CM}} \tag{A.1}$$

Here $\tilde{\varepsilon}_{mix}$ and $\tilde{\varepsilon}_{med}$ denote the complex permittivity of the mixture and medium, ϕ represents the volume fraction of the particles compared to the medium in the detection volume and $\tilde{f}_{CM}$ stands for the Claussius-Mossiti factor:

$$\tilde{f}_{CM} = \frac{\tilde{\varepsilon}_p - \tilde{\varepsilon}_m}{\tilde{\varepsilon}_p + 2\tilde{\varepsilon}_m} \tag{A.2}$$

$$\tilde{\varepsilon}_p = \varepsilon_0\varepsilon_p - \frac{j\sigma_p}{\omega} \tag{A.3}$$

$$\tilde{\varepsilon}_m = \varepsilon_0\varepsilon_m - \frac{j\sigma_m}{\omega} \tag{A.4}$$

Where ε_i and σ_i are the relative permittivity and conductivity of the particle and medium. $j^2 = -1$ and ω denotes frequency. The subscripts "p" and "m" refer to particle and medium, respectively. The clausius-Mossoti factor $\tilde{f}_{CM}$ describes the frequency-dependent effective dipole moment.

$$Z_{mix} = \frac{1}{jw\tilde{\varepsilon}_{mix}G} \tag{A.5}$$

$$\tilde{\varepsilon}_{mix} = \tilde{\varepsilon}_{med}\frac{1 + 2\phi\frac{\tilde{\varepsilon}_p - \tilde{\varepsilon}_m}{\tilde{\varepsilon}_p + 2\tilde{\varepsilon}_m}}{1 - \phi\frac{\tilde{\varepsilon}_p - \tilde{\varepsilon}_m}{\tilde{\varepsilon}_p + 2\tilde{\varepsilon}_m}} \tag{A.6}$$

After substitution of $\tilde{\varepsilon}_{mix}$ in equation A.5 and a few derivative steps and manipulations the following expression for the impedance of the mixture is formed:

$$Z_{mix} = \frac{g}{A}\frac{1}{j\omega\varepsilon_\infty + \sigma_0 + \frac{j\omega\delta\varepsilon}{1+j\omega\tau}} \tag{A.7}$$

Interestingly this equation shows resemblance with the equations that describe the behaviour of a parallel circuit of a capacitor, resistor and another contribution in parallel:

$$Z_{circuit} = \frac{1}{j\omega C_1 + \frac{1}{R_1} + \frac{j\omega C_2}{1+j\omega C_2 R_2}} \tag{A.8}$$

B Neural network classification theory

All the processed data that is acquired from each particle or cell is labeled and used to train a simple neural network algorithm. The network is trained through classifiers, which are functions that decide whether an input belongs to a certain class.

The algorithm, also called a perceptron, is a feed-forward network that starts with multiplying the input values with their (random) assigned weights. A weight, is a parameter that scales the values of the inputs. The values of these multiplications are then summed up in the weighted sum. The weighted sum is applied to an activiation function with the form of a hard limit function that returns an output of a 0 or 1.

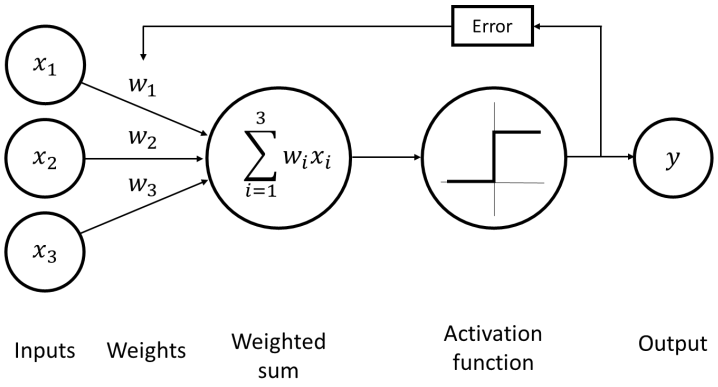

Figure B.1: Perceptron neural network with three input vectors, their assigned weights, the weighted sum, the hard-limit activation function, the error from the target that adjusts the weights after each loop, and finally one binary output

The algorithm uses an hard-limit threshold activation function that maps an input $\boldsymbol{x}$ to an output value y

$$y = \begin{cases} 1, & \text{if } \boldsymbol{w} \cdot \boldsymbol{x} + b > 0, \\ 0, & \text{if } otherwise, \end{cases} \tag{B.1}$$

Where $\boldsymbol{w}$ is a vector of weigths, $\boldsymbol{w} \cdot \boldsymbol{x}$ is the dot product $\sum_{i=1}^{n} w_i x_i$, with n being the number of inputs and b is the bias. The bias is a constant that allows the classification boundary to shift away from the origin and is independent from the input.

The hard-limit transfer function gives the perceptron the ability to classify input vectors by dividing the input space into two regions. Figure B.3 shows a problem with two classes with two inputs ($\boldsymbol{x_1}$,$\boldsymbol{x_2}$. The perceptron algorithm finds a line that correctly separates the two classes by tweaking the weights and biases after each loop. The procedure of adjusting the weights after each loop is governed by the "learning rule". In the case of supervised learning, the learning rule is given a training set where the inputs are given a corresponding target output:

$$\boldsymbol{\{x_1, t_1\}, \{x_2, t_2\}, \{x_3, t_3\}} \tag{B.2}$$

As the inputs are inserted into the network, the output is compared to the target. The learning rule then adjusts the weights and biases of the network based on the difference between the target and output, which is the error. This way the network brings the outputs closer to the

target. The limitation of this perceptron algorithm is that it can only separate input vectors that can be separated by a linear boundary.

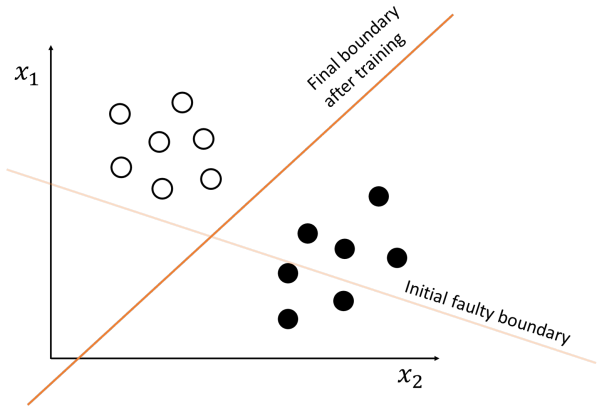

Figure B.2: The algorithm starts out with an line constructed with random weights and bias. After each loop the weights and biases are adjusted to minimize the error and readjust the line until convergence

If the output of a perceptron applied as the input for another perceptron, a multilayer perceptron is created. Unlike the single-layer, a multilayer network with non-linear transfer functions can solve arbitrary classification problems and not just classifying linearly separable patterns. This network consists of 3 or more layers, an input layer, a hidden layer and an output layer. Each node in the hidden layers represents an activation function.

Similar to a normal perceptron, in a multilayer perceptron, the learning process is carried out through backwards propagating of errors. In a multilayer network the backpropagation step takes the derivatives of the squared error with respect to the weights and biases in the hidden layers [61]. These derivatives are computed at the last layer of the network, and then propagated backward through the network, using the chain rule, to compute the derivatives in the hidden layers.

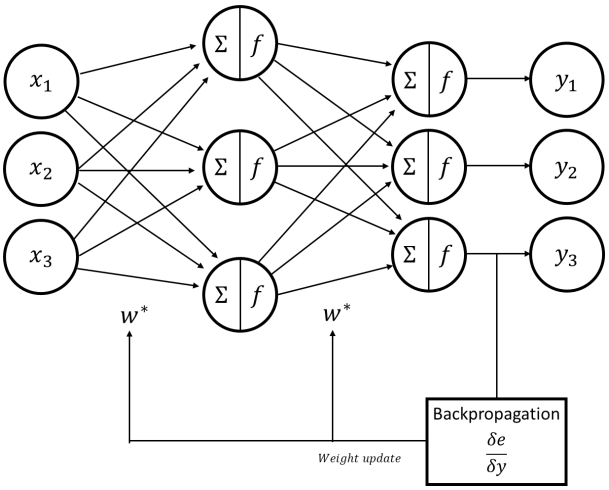

Figure B.3: The algorithm starts out with an line constructed with random weights and bias. After each loop the weights and biases are adjusted to minimize the error and readjust the line until convergence

B.1 Results of neural network with healthy and nectrotic cells

Figure B.4 shows the ROC curve. This is a graphical plot showing the diagnostic quality of the classifiers. The closer it gets to the top-left corner, the better the performance. There are several parameters describing the quality of the network. For example the true positive rate(TPR):

$$TPR = \frac{TP}{P} = \frac{TP}{TP + FN} = 1 - FNR \tag{B.3}$$

Where TP is the true positive, TP is true positive and FNR is the false positive rate.

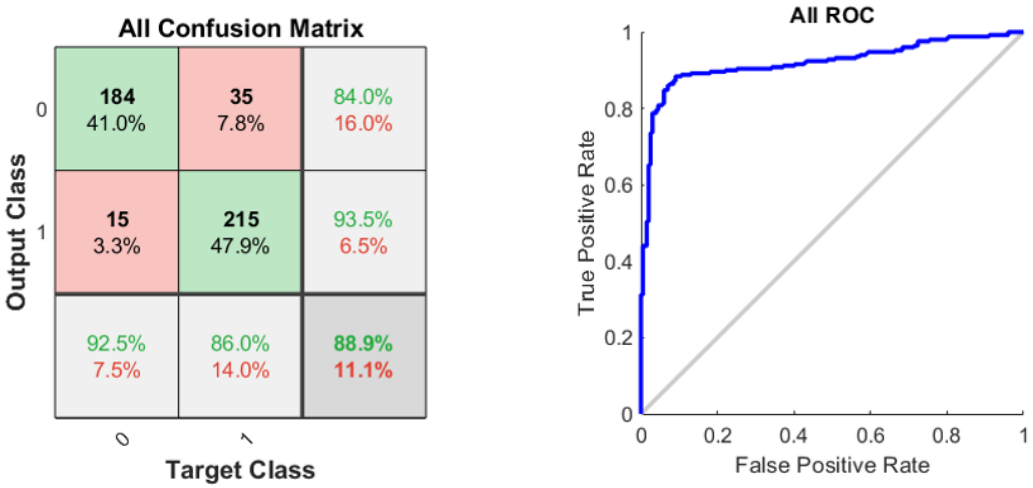

Figure B.4

C The COMSOL multiphysics model

Here we will discuss the model parameters and the results. The model was solely created with the AC/DC module. This model does not account for any influences of fluid flow dynamics, capacitive double layers around the electrode or particles. An auto generated in-depth COMSOL report of the model, where all conditions and governing equations are given, can be found here: link

It is important to know that the values of the simulation differ from the actual experimental values. As such the simulation results should be used solely for the purpose of finding trends.

C.1 Geometry

2D and 3D models were created, where geometry was changed depending on the investigated parameters. The channel lenght is between 0.25mm and 1 mm. The channel height and depth (for 3D) were 50 micrometer. The electrodes are modelled as a very thin, 1 micrometer thick, strip of gold. The Particle was modelled as a sphere with a radius of 5 micrometer. Additionally, a model for a differential setup was analyzed, where an additional third electrode was added.

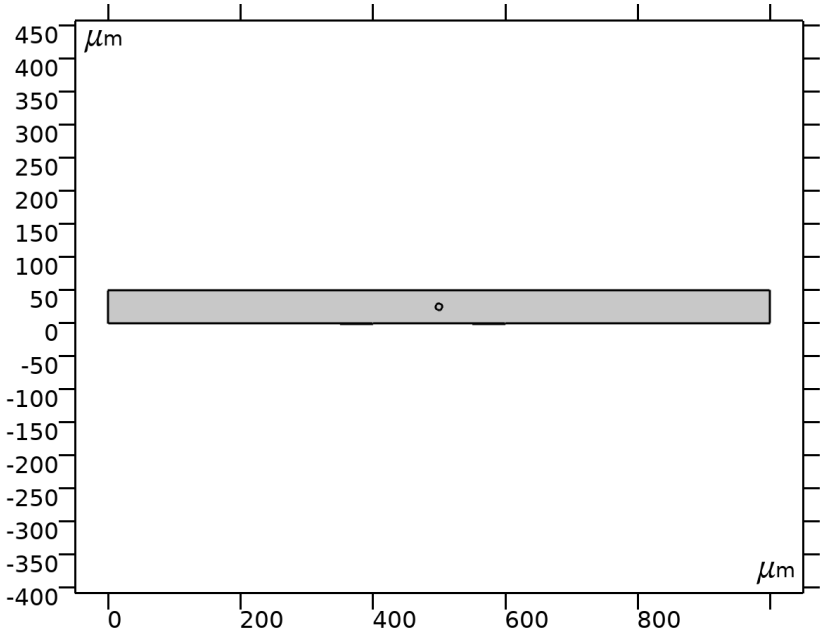

Figure C.1: 2-electrode model geometry

C.2 Materials

For the simulations, the permittivity and electrical conductivity are the most important properties. The electrodes were modelled as gold, the medium properties correspond with PBS and the sphere corresponds with polystyrene.

C.3 Physics

The electric currents module in the AC/DC module was used to insert all the boundary conditions. The study revolves around low frequency impedance analysis, 10KHz. First of all, current conservation was applied to all domains. Next, electric insulation was applied to all the edges of the channel and the electrodes. Initial values of 0 V were applied to all domains before

Component	Property	Unit
Electrode	Electrical conductivity	45.6e6[S/m]
	Relative permittivity	6.9
Medium	Electrical conductivity	1.6 [S/m]
	Relative permittivity	80
Bead	Electrical conductivity	5e-6 [S/m]
	Relative permittivity	2.55

assigning the ground and terminal conditions. The left electrode was assigned as the terminal electrode where a current of 1 Ampere was applied over the top side of the electrode surface boundary. The right electrode top surface acts as the ground electrode.

C.4 Mesh

A physics-controlled mesh was applied to the model consisting of medium sized triangular elements. The coarseness was automatically changed to fine around the electrodes, and rougher at the left and right edges of the channel.

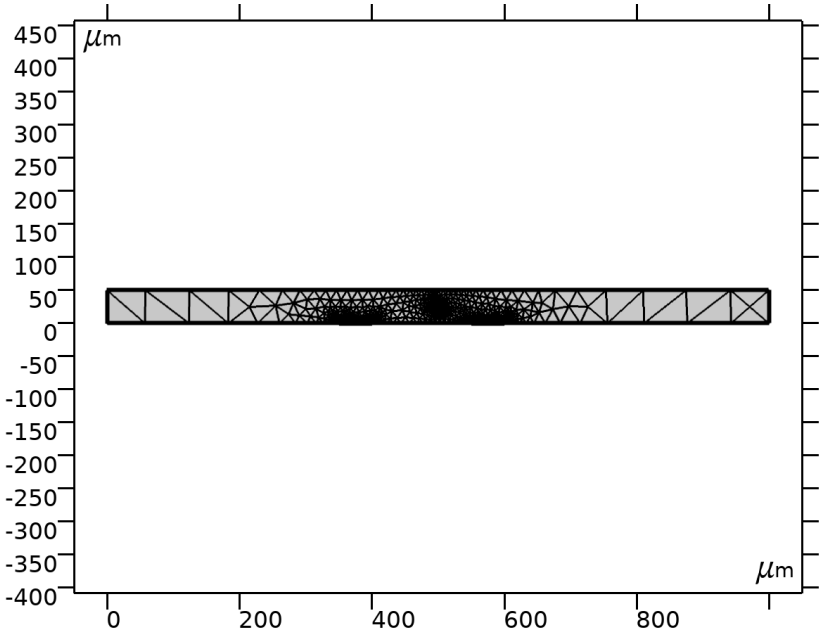

Figure C.2: Triangular mesh of the model

C.5 Study

Parametric sweeps are used to over the course of several steps translate the particle through the channel and recalculating the resulting electrical properties. Parametric sweeps are also applied to change parameters such as electrode width, electrode distance, particle sizes, particle properties and medium properties in incremental steps.

C.6 Results

A 3 model depicting the electric potential in the channel for 2-electrode and the differential model is given in figure C.3. Figure C.5 shows the current lines.

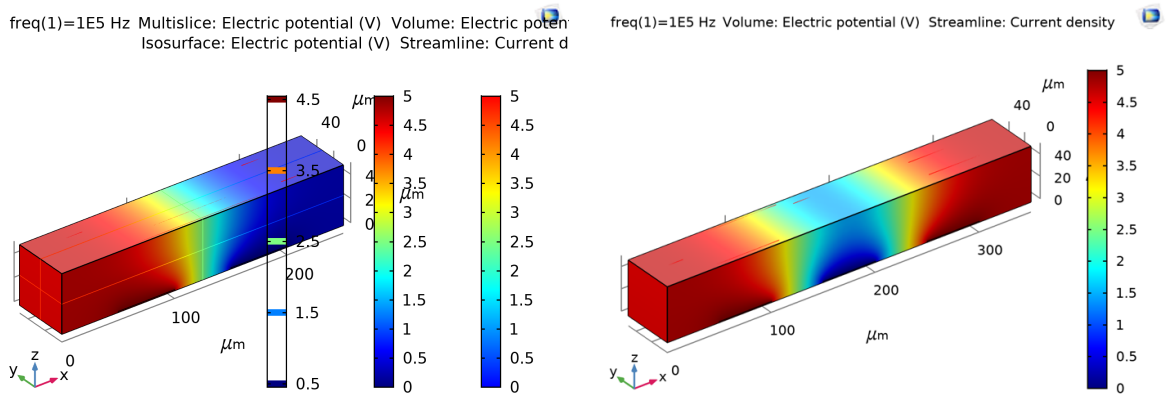

Figure C.3: Electric potential for the 2-electrode and differential setup

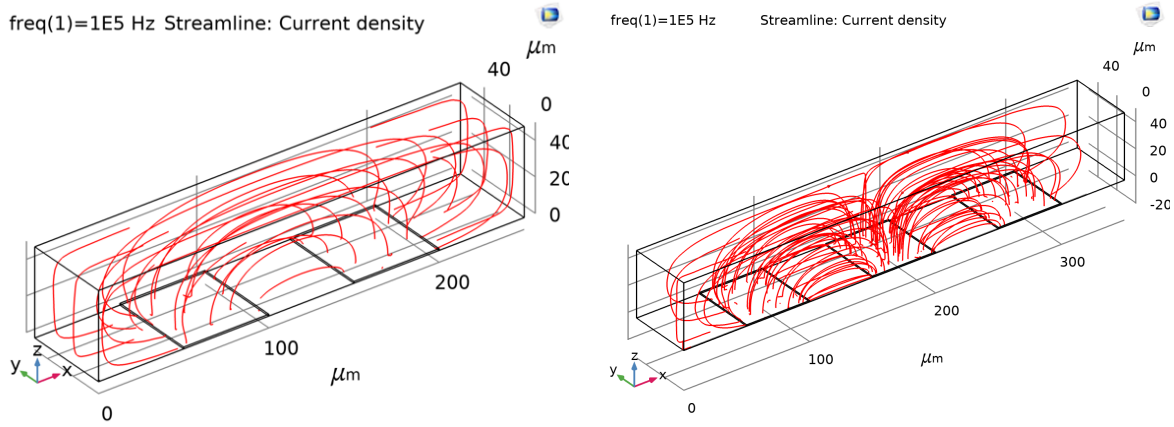

Figure C.4: Streamlines for both the 2-electrode and differential setup

C.6.1 size dependence

The next part shows the resulting change in signal measured at the second electrode, when a parametric sweep is used to translate the particle in steps of 10 micrometer through the channel and over the electrodes. Figure **??** shows the difference in signal change for differently sized beads.

C.6.2 particle trajectory height

Figure 3.1b shows the effect of particle trajectory height on the measured signal at the ground electrode.

C.6.3 electrode distance

When investigating the distance of the electrodes, it becomes very interesting. Figure **??** simultaneously shows the effects of the electrode distance d_{el}, particle height trajectory, and particle size on the voltage variation. Noteworthy is the increased signal variation that scales with the sphere volume and the significantly higher signal variation for a d_{el} of 50 μm compared to a d_{el} of 150 μm. The fact that besides the width of the peak being much wider for a larger

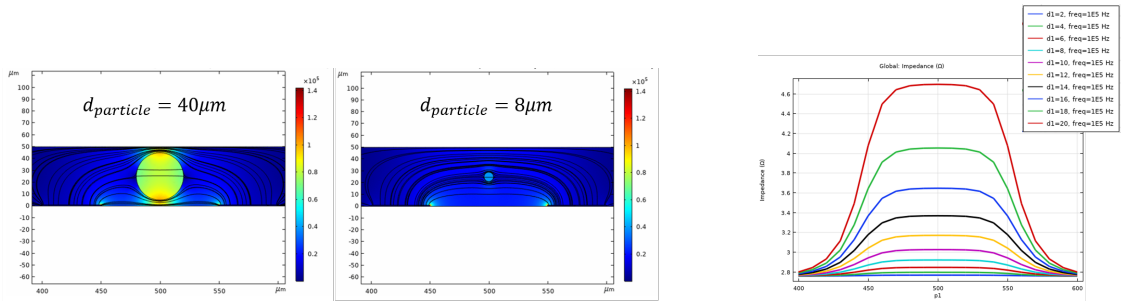

Figure C.5: (a) shows the difference electric field density and current lines as the particle size is increased. (b) shows the change in signal measured at the ground electrode

d_{el}, a larger d_{el} decreases the sensitivity to particle trajectory height. The signal variation in the central zone (x=0 μm) varies little and hence will be depend mostly on the size of the particle. To a degree, by increasing the electrode width, the positional dependence on the signal could be neutralized.

C.6.4 Particle properties

Next, we investigate the resulting changes in measured signal at the electrode as the particle properties are changed. Here the electrical conductivity is step-wise increased, see figure C.7 and figure C.6.

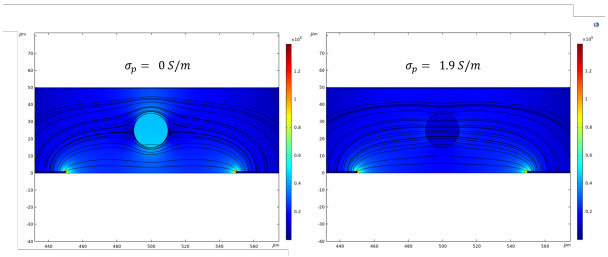

Figure C.6: Shows the change as the conductivity of the particle is changed. As the conductivity increases and averages the medium conductivity, the current lines pass through the bead instead of the medium

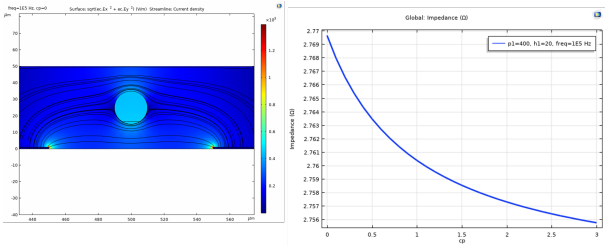

Figure C.7: Shows the change as the conductivity of the particle is changed. As the conductivity increases and averages the medium conductivity, the current lines pass through the bead instead of the medium

C.6.5 Channel height

The biggest influence on the sensitivity is expected to be the ratio of the particle volume to the detection volume. To simulate this, the height of the channel is decreased incrementally. There

we show the increae in signal as the channel height is reduces in steps. This is shown in figure C.8, where the resulting signal change is decreased as the channel height is increased.

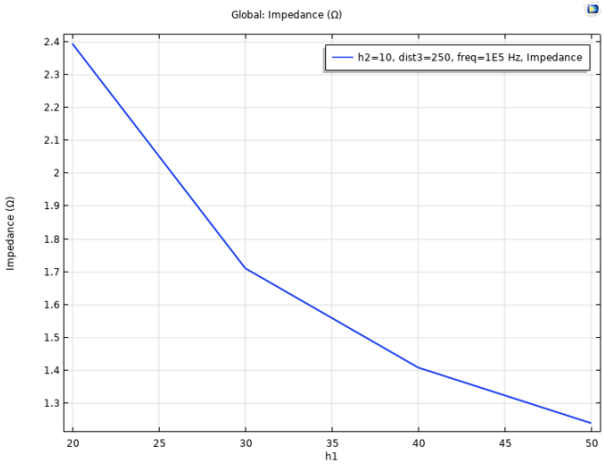

Figure C.8: On the x-axis the channel height increase vs the impedance change as the particle passes the channel

C.7 Double particles

When 2 particles pass through the channel, a coincident event occurs, mostly reulting in an a-symetrical peak. Figure C.9 shows the a-symetrical peaks when two particles (not exactly above each other, pass the electrodes at the same time. This double peak can be used in the future as a sign of coincident particles.

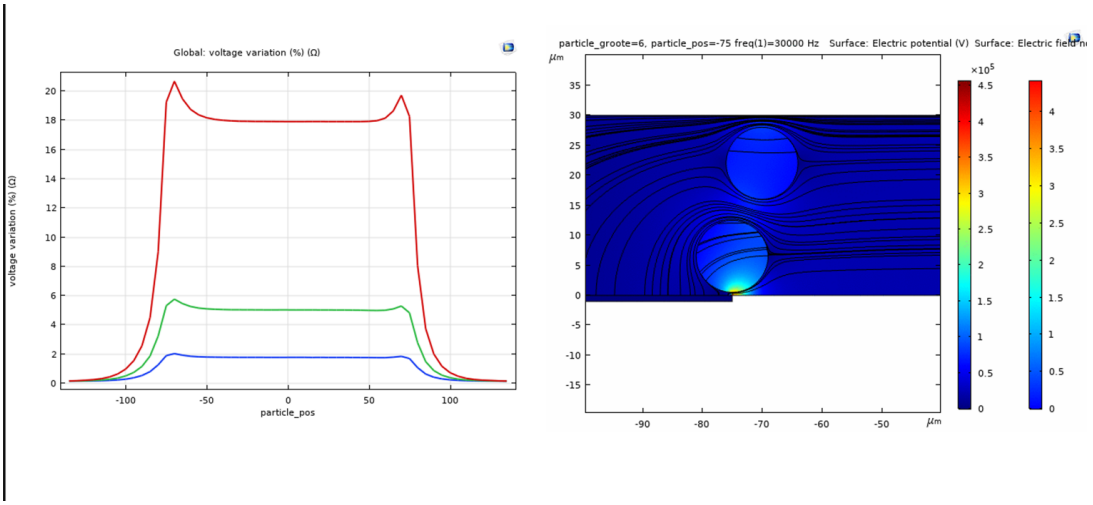

Figure C.9: A-symmetric peaks for double coincident particles passing the electrodes

D Electro-chemical Impedance Spectroscopy

Impedance spectra of the devices were created with an EIS measurement using a potentiostat (BiologicSP-150). The principle of Electrochemical Impedance Spectroscopy (EIS) is to apply a small alternating potential to the system, and to measure how the systems responds to these small signals at the steady state. The amplitude is very small (10mV) in order to assume the linear behaviour of the system.

The experiments were done in 3 electrode configuration. One of the elctrodes of the device is chosen as a working electrode. The neighbouring electrode is connected as a counter electrode. An independent reference electrode of Silver/Silver Chloride (Ag/AgCl) is inserted in one of the channel entrances. Because the reference electrode is relatively far away from the working- and counter-electrode, the measurements are not perfectly comparable with the impedance measurements with the lock-in amplifier, though still useful to detect trends. Experiments where the channel was filled with tapwater, purified water, PBS, NaCl enriched tapwater and PBS-bead mixtures were tested.

E Data analytics

E.0.1 signal conditioning

In order to analyze the raw data generated by the lock-in amplifier, signal conditioning is a crucial step in order to make it decipherable. In this case conditioning of the signal encompasses amplification, filtering and denoising.

When a large particles passes the electrodes, naturally the signal change is large, simplifying distinction. However, with smaller particles, the resulting signal changes are small and therefore makes it essential that the baseline be smooth and free of noise and drift. Recorded data streams always exhibit some noise and baseline drift which is caused by all kinds of factors. In order to improve the signal quality, denoising and detrending is applied.

Baseline noise is the short time variation of the baseline from a straight line. From an electrical point of view, a major part of the noise contribution in the frequency range of interest is due to the thermal noise in the channel and the noise generated by the equipment and cabling. [72]

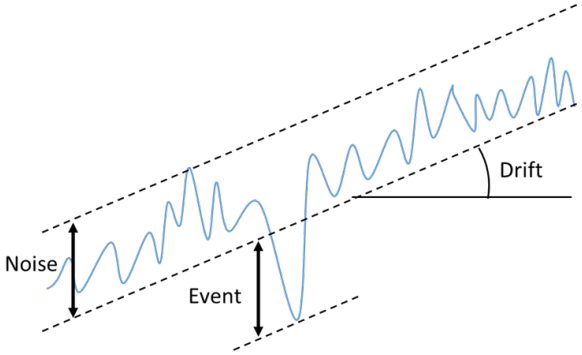

Figure E.1

To compensate for signal drifting and at the same time implement normalization, two methods are explored. The first being a baseline fit that is interpolated from selected points and then applied to the data. The second is a method where a series of averages of segments is created and is subsequently subtracted from the original signal (moving average). These methods are obviously not perfect and result in some loss of peak information. Especially the areas in the signal where the throughput is high.

To compare, figure E.3a and figure E.3b show a raw magnitude signal with a fitted baseline based on interpolation and the moving average method respectively. This particular temporal area in the measurement shows a relatively high density of peaks, meaning a high particle throughput and relatively more artefacts due to coincident particles, which results in lower fitting quality. For both methods a certain segmentation length has to be chosen over which there will be interpolated/averaged. The segmentation length has a big impact on the fit quality and should be chosen strategically. Short segmentation length can incorporate abrupt baseline changes, but increases the chance of an end point landing exactly on a peak/valley. Whereas larger segments lose information of abrupt baseline changes but decreases the chance of an end point landing exactly on a peak/valley. It is concluded that generally short segmentation lengths are suitable for eventful high throughput measurements, and larger segmentation lengths improve the baseline fit of uneventful portions. 10.2 shows a comparison between the interpolation and moving average method by means of standard deviation in average peak heights. Extensive

visual inspection of baseline fit quality and a lower deviation in peaks show that the moving average method is the most suitable method for analysis of raw signals.

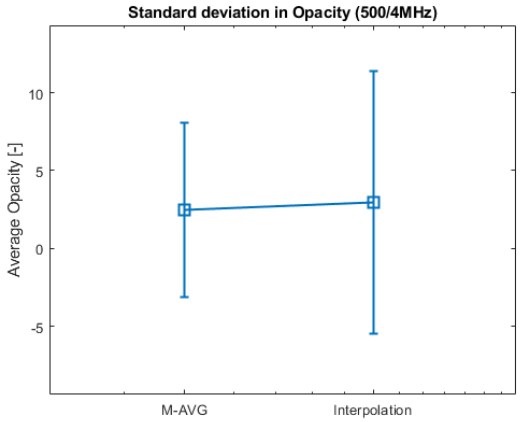

Figure E.2: plots of the raw magnitude signal with substantial change in noisefloor with a fitted baseline. (a) baseline fit using the Piecewise Cubic Hermite Interpolating Polynomial (PCHIP) method. (b) uses a moving average baseline fit

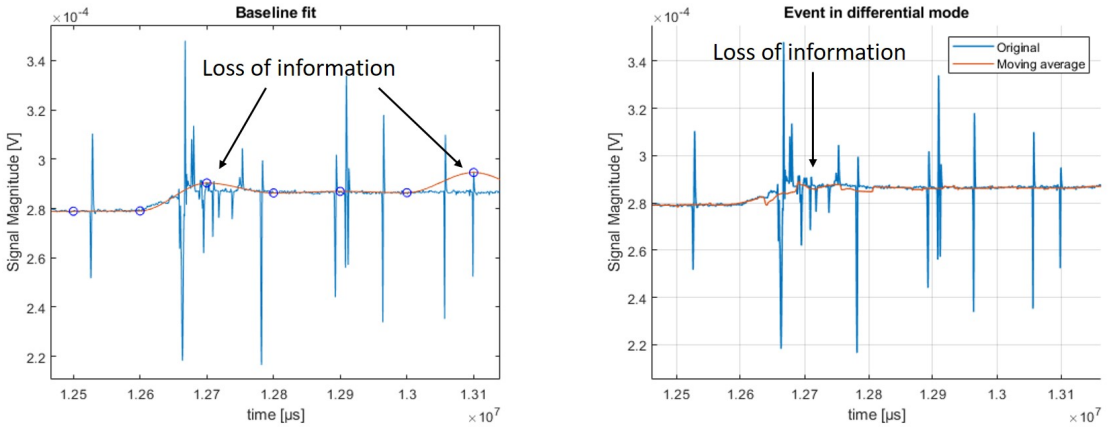

Figure E.3: My figure with side subcaptions

By using the two-electrode setup A differential configuration with three coplanar electrodes makes it possible to measure the difference in signal between the two outer electrodes. As a cell passes through the electrode gap, one pair is used for sensing the current change, whilst the other pair provides a reference. With this configuration the background noise is significantly reduced and therefore an improved signal to noise ratio and sensitivity is achieved.

Another advantage derives from the fact that the measurement and reference electrodes are inherently switched; any uneven drift of the electrode properties can be sensed and corrected, as both signal maxima should be of the same amplitude. The signal from a differential setup.

E.1 feature extraction

Once the raw signals have been properly preprocessed, it is ready for peak finding i.e. extraction of significant changes in the raw signal. There are a variety of strategies to extract relevant

information, for example peak finding through thresholding, derivative-based approaches and template fitting [74]. However, there is always a compromise between computational cost and accuracy.

The most straight forward, time efficient and cost-effective way of extracting data is threshold based peak finding. This means that if a peak in the baselined signal reaches a certain threshold it is classified as an particle event, i.e. the passage of a cell or particle. Here the signal could be the real (in-phase) component, imaginary (out of phase) component, their combined magnitude, or the change in phase angle at a certain frequency.

However, threshold peak finding has some problems of its own. When synchronizing the signals of different frequency a problem arises: for an event at low frequency there is a peak in magnitude. At higher frequencies this might be a inverse peak. By using just a simple threshold for each frequency, this would lead to a peak at low frequency being coupled with a peak at another (wrong) location at higher frequencies. Especially with differential measurements there is a high chance of erroros, see figure... To visualize, using the complex plane of the impedance, if the baseline signal is close to the origin and an event would make the signal cross the origin. The phase would abruptly change with 180 degrees. The magnitude would change to another value as well. This would lead to artefacts and corrupted data. Therefore it is important to choose the a frequency where this phenomena does not occur.

For higher frequency the baseline signal is also higher. This is due to the electromagnetic pickup scaling with frequency and becoming more dominant for higher frequency. This means that for increased frequencies it is more important to use improved shielding for the device from the environment.

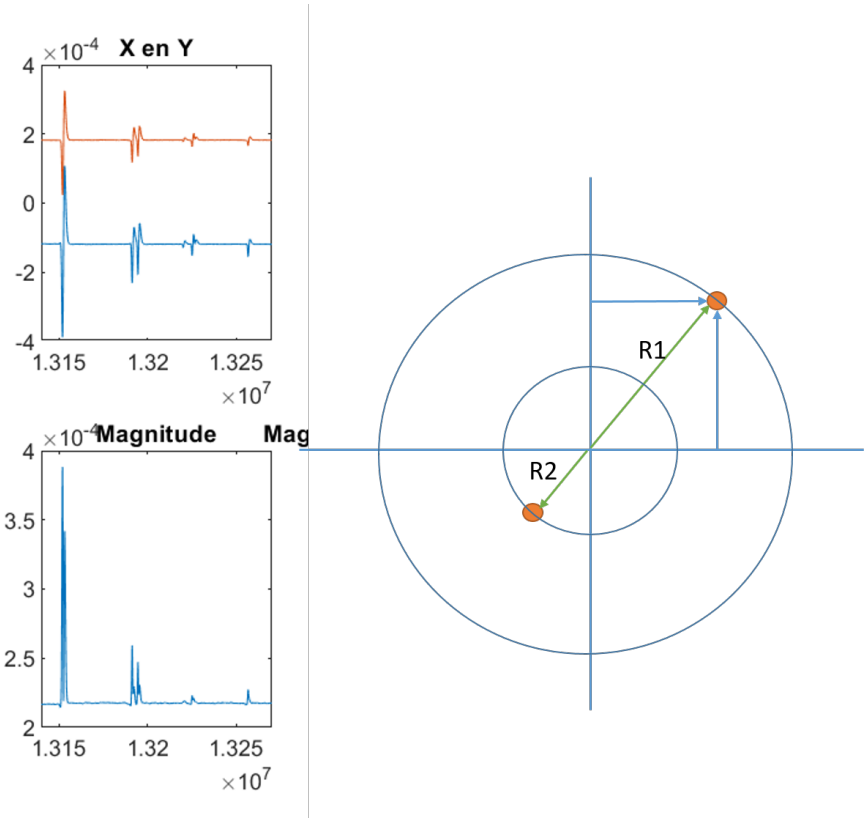

Figure E.4: Occurance a "Double peak"

F Additional experiments

F.1 Device characterisation

Figure F.1 shows additional experiments where differently sized polystyrene beads were measured at different frequencies with single electrode pairs and in differential configuration. As expected, with the differential configuration the overall performance is improved. The reduces scattering is explained by a measurement that is more independent from environmental changes and thus more precise and accurate measurement. figure F.1 and F.2 shows the opacity. It is noteworthy that the opacity of the differently sized beads differ from each other, as the material is simillar. These beads were measured in separate experiments, which could account for the difference in opacity. If beads are mixed in one mixture, the beads show the same opacity.

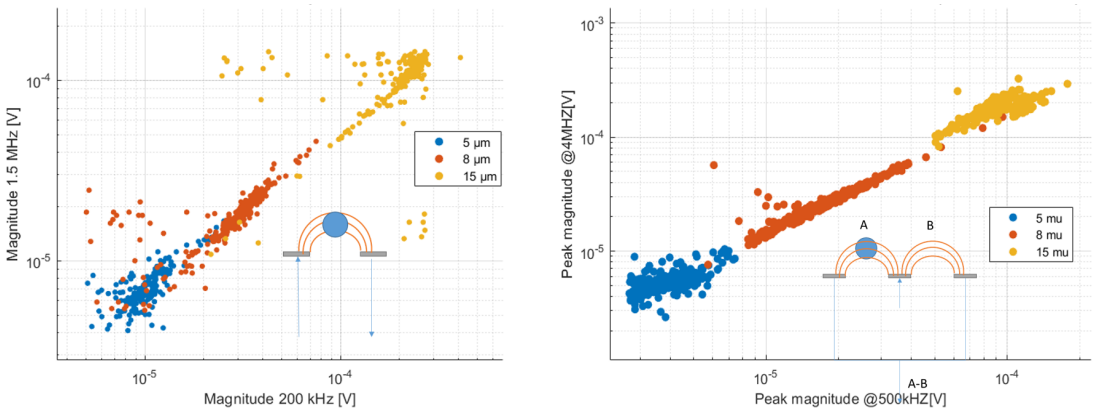

Figure F.1: Comparison between differential and single electrode pair configuration

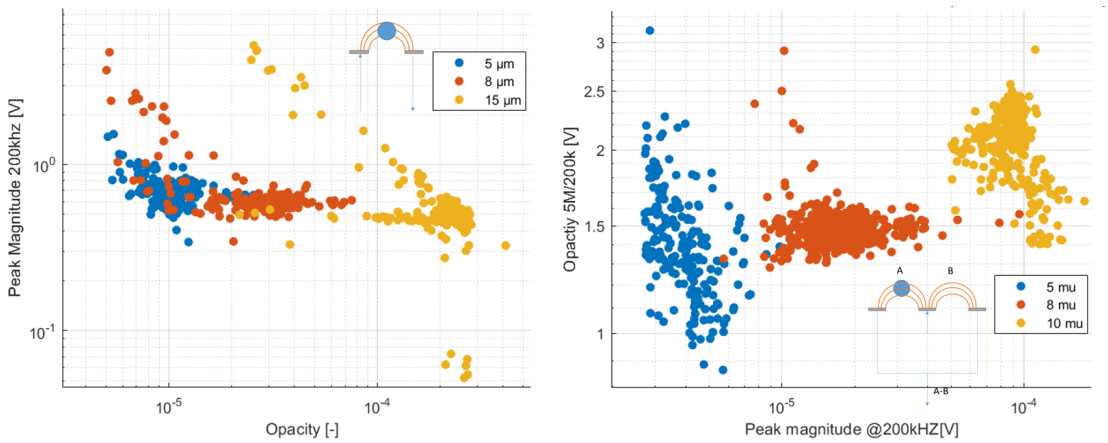

Figure F.2: Comparison between differential and single electrode pair configuration

F.2 spectrum analysis

Additional sweeps where the particle was located in the middle between two electrodes were performed. Here different cells and particles were measured. Notice the difference in slope for the polystyrene beads and the cells in figure F.3

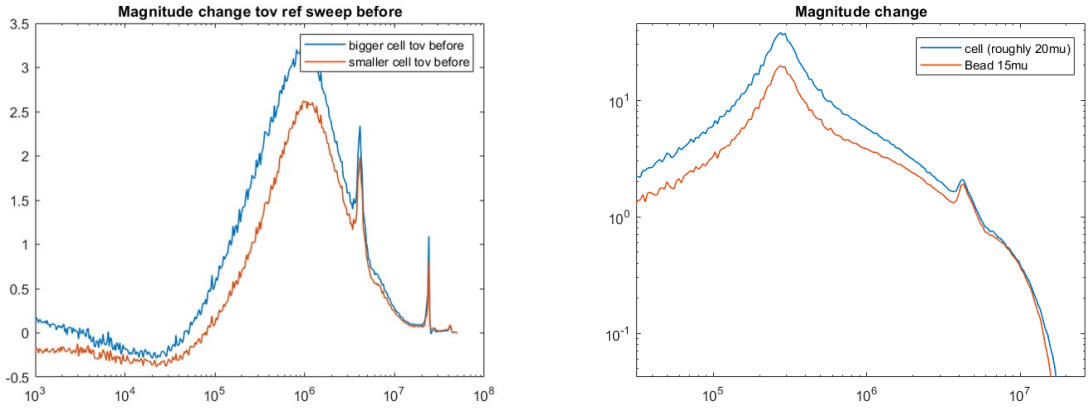

Figure F.3: Sweeps with differently sized beads in detection area.(a)Magnitude vs frequency (b) Phase vs frequency.

Figure F.4 shows the impact of the differential configuration compared to the single electrode pair measurements. It shows the sweep with solely PBS, corresponding with the background signal. With differential mode the background is significantly reduced.

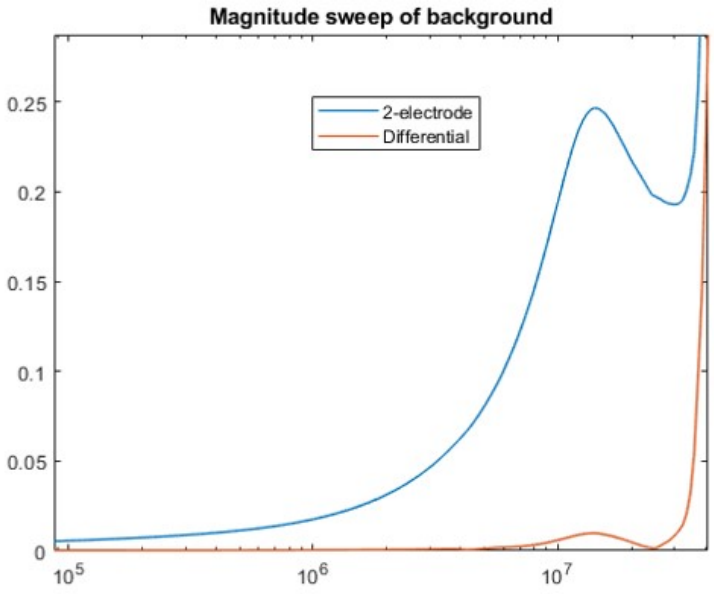

Figure F.4: Sweep with with 1-electrode pair and in differential configuration(3-electrodes)

F.3 additional cell experiments

Many experiments featuring MCF-7 and MDA-cells were conducted. In figure F.5 an experiment with MCF-7 cells and polystyrene beads is depicted. The data was labeled with optical imaging. Interesting is that certain cells light up, or reflect the light in a different way. This might indicate the vertical position of the particle.

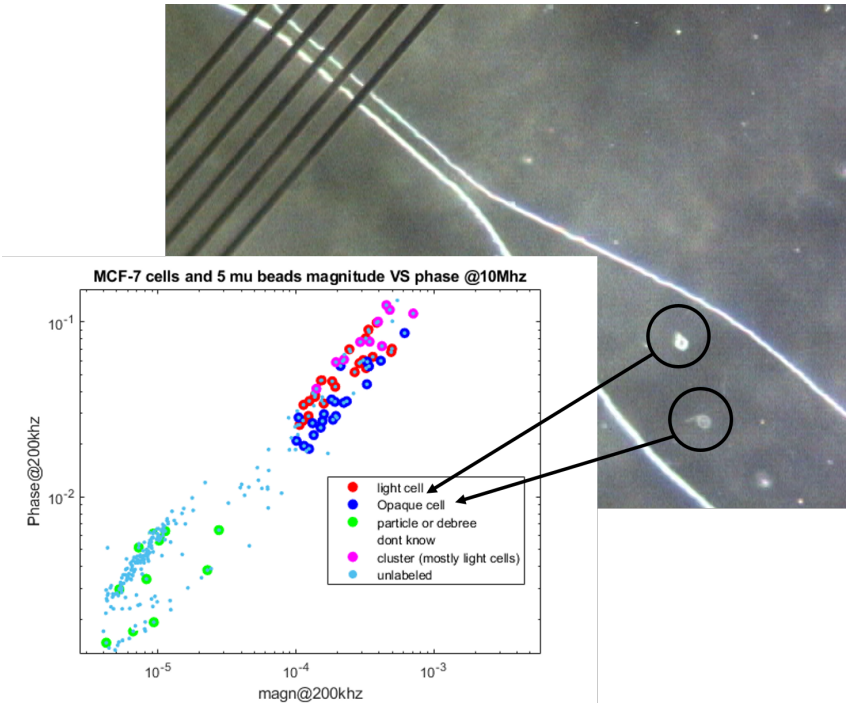

Figure F.5: Experiment with MCF-7 cells and polystyrene beads labeled with optical imaging

Figure F.6 shows a simple impedance magnitude versus transit time plot, where MCF-7 cells and differently sized beads are combined.

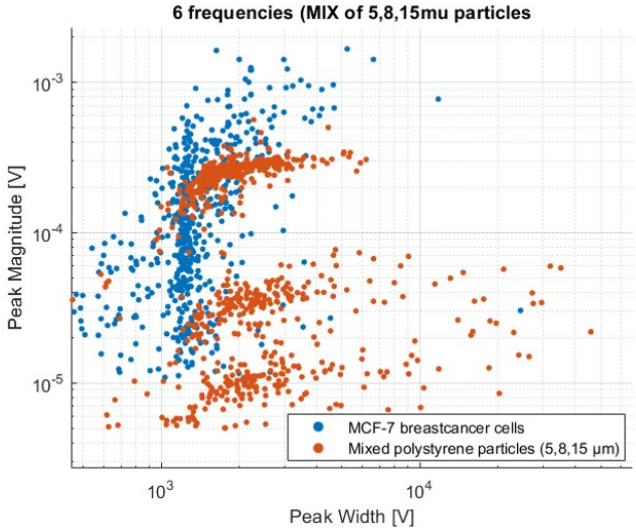

Figure F.6: impedance magnitude versus transit time plot, where MCF-7 cells and differently sized beads are combined.

G Images & Video's

Figure G.1 is a QR code for a short video showing a mixture of MDA-M23 breastcancer cells and 5 μm polystyrene beads.

Figure G.1: QR code of a short video

Figure G.2 displays the renders compared with the actual device.

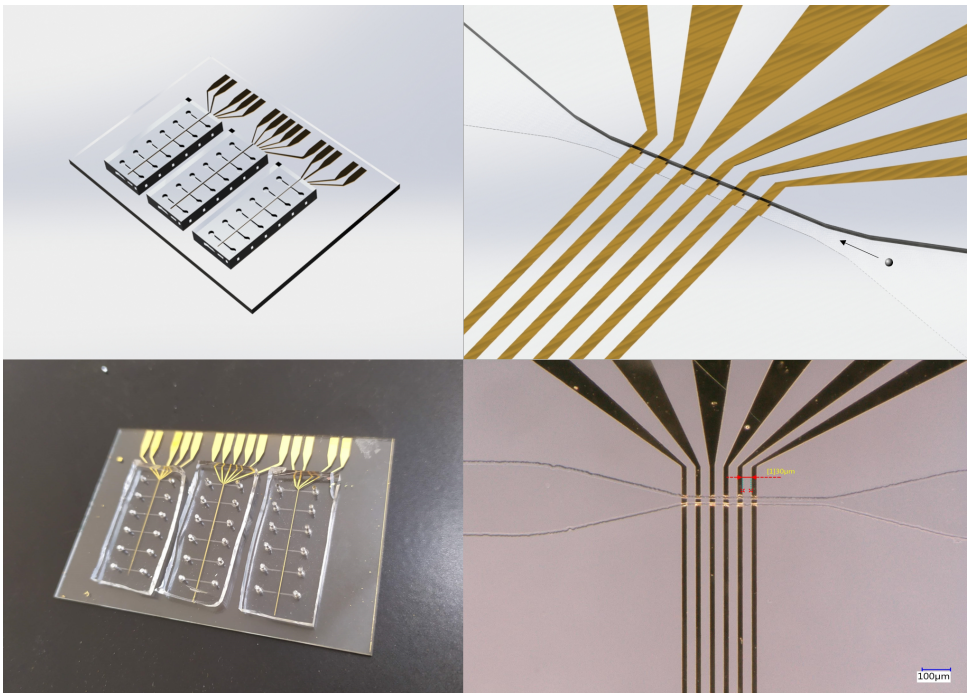

Figure G.2: Comparison of the device renders and the actual device

H Additional information on the setup

Table H.1

Component	Type	Manufacterer
Microscope	inverted microscope	Olympus
Camera	DFK 23UP031	Imagingsource
Chip holder	Clamp with soldered cabling	Unknown
Lock-in amplifier	HF2LI 50 MHz Lock-in amplifier	Zurich Instruments
Syringe pump	Nexus 3000	Chemyx
Pressure driven pump		Fluigent

I Declaration TU/e Code of Scientific Conduct for the Master thesis

Technische Universiteit
Eindhoven
University of Technology

Declaration concerning the TU/e Code of Scientific Conduct for the Master's thesis

I have read the TU/e Code of Scientific Conduct[i].

I hereby declare that my Master's thesis has been carried out in accordance with the rules of the TU/e Code of Scientific Conduct

Date

08-06-2021

Name

Joris Leonardus Dijcks

ID-number

1069276

Signature

Submit the signed declaration to the student administration of your department.

[i] See: http://www.tue.nl/en/university/about-the-university/integrity/scientific-integrity/
The Netherlands Code of Conduct for Academic Practice of the VSNU can be found here also.
More information about scientific integrity is published on the websites of TU/e and VSNU